Tracing metallic pre-concentrations in the Limousin ophiolite-derived rocks and Variscan granites (French Massif Central)

Afifé El Korh, Marie-Christine Boiron, Michel Cathelineau, Etienne Deloule, Béatrice Luais

To cite this version:

Afifé El Korh, Marie-Christine Boiron, Michel Cathelineau, Etienne Deloule, Béatrice Luais. Tracing metallic pre-concentrations in the Limousin ophiolite-derived rocks and Variscan granites (French Massif Central). Lithos, 2020, 356-357, pp.105345. 10.1016/j.lithos.2019.105345 . hal-02735233

HAL Id: hal-02735233
https://hal.science/hal-02735233v1

Submitted on 2 Jun 2020

Tracing metallic pre-concentrations in the Limousin ophiolite-derived rocks and Variscan granites (French Massif Central)

Afifé El Korh[1]*, Marie-Christine Boiron[2], Michel Cathelineau[2], Etienne Deloule[1], Béatrice Luais[1]

[1] Centre de Recherches Pétrographiques et Géochimiques (CRPG), UMR 7358 CNRS-Université de Lorraine, 15 rue Notre Dame des Pauvres, BP 20, F-54501 Vandœuvre-lès-Nancy Cedex, France
[2] Université de Lorraine, CNRS, GeoRessources, F-54000 Nancy, France

* Corresponding author:
Present address: Unit of Earth Sciences, Department of Geosciences, University of Fribourg, Chemin du Musée 6, CH-1700 Fribourg, Switzerland
E-mail: afife.elkorh@unifr.ch

Abstract

The French Massif Central (FMC) is part of the West European Variscan belt. The economic and sub-economic ore deposits from the Limousin area are the consequence of intensive fluid-rock interactions related to a lithospheric delamination process that occurred during the Neo-Variscan Period (320–290 Ma). This study focuses on the fingerprints of fluid-rock interactions in the Limousin ophiolite-derived rocks and granitic massifs, in order to trace the source of trace elements transported by fluids involved in the formation of the Variscan ore deposits (including

Sn, W, Au and U deposits). A series of compatible and incompatible metallic trace elements (Ag, As, Au, Bi, Li, Co, Cr, Cu, Ga, Ge, Ni, Pb, Sb, Sc, Sn, Ti, V, W) were analysed in a series of basic (metagabbros, basic dykes), ultrabasic (serpentinites) and felsic (granites and gneisses) rocks, as well as in the mineral assemblages, in order to determine their relationships with the Limousin ore deposits.

Serpentinites and their mineral assemblages (serpentine, olivine, amphibole, chlorite and spinel) show high concentrations in compatible transition metals (Sc, V, Cr, Co, Ni, Zn, Cu) and low abundances of incompatible metals (Ge, Ga, Mo, Sn, Sb, W). Associated amphibolites (metagabbros and metamorphosed dykes) show high contents of compatible metals, though lower than ultrabasic rocks. Amphibole and, to a lesser extent, titanite, are the main hosts for metallic trace elements. Abundances in incompatible metals are generally low. Amphibole has low Sn and Sb contents, while higher Sn contents were measured in titanite. In a UHP zoisite-eclogite cropping out close to one of the ophiolite-derived massifs, zoisite, rutile, omphacite and retrograde amphibole show high concentrations of incompatible elements (Sn, Sb, W, As, Ga, Ge, Mo and Bi). However, it has been shown that high-temperature and low-temperature hydrothermal alteration that have affected the basic and ultrabasic protoliths is c. 100 Ma older than those that were responsible for the formation of ore deposits. For this reason and as well because of their low W and Sn abundances, the ultrabasic and basic rocks cannot be considered as source for the Limousin W–Sn ore deposits.

In granite and gneisses, the metallic trace elements are mainly hosted by biotite and muscovite. Quartz and feldspars only show minor amounts of Sc, Ga, Ge, Sn and Pb. The micas contain low amounts of Ge, As, Sb, Bi and variable amounts of Sc, Cu and Ga. Besides, micas display significant Sn and W contents. Variations in Sn and W in micas allow tracing the pre-mineralisation concentrations in the granitic massifs: there is a clear geographical correlation between the Sn and W composition of micas and the importance of the W–Sn ore deposits, arguing for a local source of pre-concentrations. Granites from the Vaulry W–Sn ore deposit

display the highest W and Sn concentrations, while granites hosting the Au deposits in the southern part of the Limousin (St-Yrieix, Cheni, Lauriéras) show the smallest concentrations.

Keywords

Trace elements; Metallic elements concentrations; serpentinites; metagabbros; granite; Variscan belt; LA-ICP-MS

1. Introduction

The French Massif Central (FMC) belongs to the internal zone of the West European Variscan belt (e.g. Matte, 2001; Lardeaux et al., 2014) (Fig. 1a). It results from a continent-continent collision between the Gondwana and Laurussia (formed of Laurentia, Baltica and Avalonia) that has started during the Devonian (c. 355 Ma), after the closure of oceanic domains and collision of continental fragments derived from the disruption of the northern Gondwana margin (Eo-Variscan stage) during the Early Palaeozoic (Cambrian-Silurian) (e.g. Ledru et al., 1989; Franke, 1992; Faure et al., 2009; Lardeaux et al., 2014; von Raumer et al., 2015; Stephan et al., 2019). Different models, partly diverging, were developed for the evolution of the Variscan orogen and Palaeozoic geodynamics. Major oceanic domains were separating the continental domains. In particular, the Rheic ocean that opened in the Cambrian–Ordovician along the continental margin of northern Gondwana was one of the most important oceanic domains during the Palaeozoic (e.g. Matte, 2001; Pin et al., 2001; Stampfli et al., 2002, 2011; Ballèvre et al., 2009; Faure et al., 2009, 2017; Nance et al., 2010; Romer and Kroner, 2013; von Raumer et al., 2013, 2015, 2016; Lardeaux et al., 2014; Franke et al., 2017; Stephan et al., 2019).

The Moldanubian Zone (or allochthonous domain; Fig. 1a) includes a series of basic and ultrabasic magmatic rocks, with an oceanic affinity. Geochronological data indicate that these rocks formed during the Cambrian-Ordovician, and are contemporaneous with to the opening of the Rheic ocean (for a review of ages, see von Raumer et al., 2013, 2015). In the Western Variscan belt, these ophiolite-derived rocks were interpreted as the remnants of a narrow ocean between Gondwana and Armorica (Matte, 2001), the "Galicia-South Brittany-Moldanubian" or "Medio-European" ocean (Matte, 2001; Faure et al., 2005; Lardeaux et al., 2014), or the remnants of a late-Cambrian active margin setting along the northern margin of the Gondwana (von Raumer et al., 2015). Other studies suggest that the ophiolite-derived rocks recognised in the Moldanubian zone correspond to the oriental branch of the Rheic ocean (e.g. Stephan et al., 2019).

Two main orogenic events are recognised in the Western Variscan belt: 1) Middle Devonian subduction of the oceanic crust under Gondwana and Laurussia; and 2) Early Carboniferous continental collision between Laurussia and Early-Palaeozoic Gondwana-derived continental terranes (e.g. von Raumer et al., 2013; Kroner and Romer, 2013; Lardeaux et al., 2014; Faure et al., 2017; Franke et al., 2017). The FMC has recorded a polycyclic evolution during the Variscan orogeny corresponding to six main tectonic-metamorphic events (e.g. Faure et al., 2009; Lardeaux et al., 2014): 1) Late Silurian high-pressure metamorphism (D_0; c. 415 Ma); 2) Early Devonian top-to-southwest nappe displacement, migmatisation and exhumation of HP rocks (D_1; 385–380 Ma); 3) Late Devonian to Early Carboniferous top-to-northwest shearing and medium pressure–medium temperature metamorphism (D_2; 360–350 Ma); 4) Visean top-to-south ductile shearing and onset of synorogenic extension in the northern FMC (D_3); 5) Early syn-orogenic extensional tectonism controlled by NW–SE stretching (D_4); 6) Late Carboniferous late-orogenic extensional tectonism controlled by NNE–SSW stretching (D_5).

The FMC is composed of five units resulting from the piling of a series of nappes during the Meso-Variscan period (Devonian-Early Carboniferous; c. 350–360 Ma; D_2 event) (Ledru et al., 1994; Faure et al., 2009): 1) the Upper Allochthon (called Thiviers-Payzac Unit or Gartempe Unit in the North Limousin), a group of low-grade Palaeozoic terranes of limited extent; 2) the Middle Allochthon (Upper Gneiss Unit; UGU; Ledru et al., 1989; Dubuisson et al., 1988; Faure et al., 2009), a composite terrane formed by the "leptyno-amphibolite complex" (LAC) (e.g. Santallier et al., 1988), an association of paragneisses, leptynites and amphibolites of medium to high grade Barrovian metamorphism, with migmatised metagreywackes and relicts of (ultra)high-pressure (UHP) eclogites (P ~ 2.9 GPa, T ~ 660°C; 412 ± 5 Ma; Berger et al., 2010) and HP granulites (Groupe I granulites; Pin and Vielzeuf, 1983); 3) the Lower Allochthon (Lower Gneiss Unit; LGU; Ledru et al., 1989; Faure et al., 2009), consisting of metasediments (paragneisses, micaschists, metashales and metagreywackes) and Late Proterozoic–Early Cambrian and Ordovician orthogneisses; 4) the "Parautochthon", made of metasediments and metagranites;

and 5) the Southern Palaeozoic Fold-and-Thrust Belt, corresponding to continental margin/platform series (e.g. Arthaud, 1970; Demange, 1994). Serpentinite and metagabbros massifs of the Limousin form a thrust sheet of ophiolite-related rocks within the Middle Allochton zones, i.e. intercalated between the UGU and LGU (Girardeau et al., 1986; Dubuisson et al., 1989; Berger et al., 2005).

Neo-Variscan stage (Late Carboniferous-Early Permian) is characterised by extensive granitic magmatism and succession of extensional tectonics, characterised by NW–SE stretching and NE–SW shortening (D_4 and D_5 events; Faure et al., 2009). Strike-slip motions resulted in E–W folding of the piled nappes and formation of major crustal-scale shear zones (Arthaud and Matte, 1975). Two exhumation stages associated with two extensional stages were recorded: 1) The first exhumation stage occurred at c. 335 Ma, i.e. at the onset of the syn-convergent extension that have followed the end of the nappe stacking (Faure and Pons, 1991; Burg et al., 1994; Faure, 1995); 2) The second exhumation stage results from the late-orogenic extension and collapse of the belt, at c. 310–305 Ma (Le Carlier de Veslud et al., 2013). A widespread basic magmatism evidenced as lamprophyre dykes and related to the ‘‘basin and range’’ extensional tectonics, also occurred during the Neo-Variscan stage (e.g. Vallance et al., 2004). Medium- to low-pressure granulite facies metamorphism due to a major thermal anomaly during the late stage of the Variscan orogeny led to the formation of migmatites, anatectic granites and granulites at the basis of the crust (Groupe II granulites; Pin and Vielzeuf, 1983).

The French Massif Central (FMC) contains numerous Variscan ore deposits, some of them being known since the gallo-roman times (Au, Ag, Pb, Sn) (Cauuet, 1999; Marignac and Cuney, 1999). Particularly, the FMC hosts important economic to subeconomic deposits of Au, U, W, Sn, Li, F, Ba, Ta, kaolin and coal, as well as minor deposits of Sb, Be, Pb, Zn, Cu and Mo (Cathelineau et al., 1990; Marignac and Cuney, 1999). Most of the Variscan ore deposits were formed during the late stage of uplift (i.e. during the Neo-Variscan stage) (Boiron et al., 1990, 1992, 2003; Marignac and Cuney, 1999; Alexandrov et al., 2000; Cuney et al., 2002).

In the Northern Limousin, important W-Sn, Au and U ore deposits were found (e.g. Boiron et al., 1989, 1990, 2003; Cuney et al., 1990; Scaillet et al., 1996a, 1996b; Raimbault, 1998; Le Carlier de Vesclud et al., 2000, 2013; Essarraj et al., 2001, Vallance et al., 2001, 2004; Harlaux et al., 2018). While most of the W-Sn deposits in the FMC are hosted by metasediments (Marignac and Cuney 1999), several minor W-Sn deposits in the Northern Limousin are hosted by rare metal peraluminous granites (RMG) (Vallance et al., 2001). Emplacement of the RMG at shallow depth (< 5 km) was associated to an intensive fracturing, which behaved as pathways for the mineralising fluids (Le Carlier de Veslud et al., 2000). Mineralised structures are vein-hosted and result from the percolation of different hydrothermal fluids during delamination process of the lower lithosphere related to exhumation of the Variscan belt (Vallance et al., 2001; Le Carlier de Veslud et al., 2013). Medium- to low-pressure granulite-facies metamorphism at the basis of the lower crust was also source of fluids, whose migration and transport were enhanced by decompression and extension processes during exhumation (Le Carlier de Veslud et al., 2000; Vallance et al., 2001).

Most U deposits correspond to fillings of faults developed in the basement and are mainly hosted by granites (e.g. Cuney et al., 1990; Cathelineau et al., 1990, 1993; Marignac and Cuney, 1999). U deposits result from multi-stage processes: 1) brittle fracturing associated to late magmatic shear zones during the Late Carboniferous magmatism triggered the release of highly fractionated uranium-rich melts and fluids, which crystallised in the late magmatic shear zones; 2) U was mobilised during hydrothermal processes related to Early Permian extensional tectonics (Cuney et al., 1990; Cathelineau et al., 1990; Marignac and Cuney, 1999). Mixing of reducing fluids derived from former overlying Permian sedimentary basins (half-grabens) and meteoric oxidising fluids (Dubessy et al., 1987) was responsible for U leaching and re-precipitation in fracture zones at low-temperature (160 ±180°C: Lespinasse and Cathelineau 1990; El Jarray 1993).

Au deposits are mostly fault-sealed by quartz, hosted by metamorphic series such as micaschists, orthogneiss, metasedimentary rocks (arkosic sandstones, limestones), as well as by granites or volcano-sedimentary rocks (Cuney et al., 1990; Boiron et al., 1989, 2003; Bouchot et al., 1989, 1997; Essarraj et al., 2001; Marignac and Cuney, 1999; Vallance et al., 2004). Au was deposited in second-order faults associated to the main shear zones, active during the Variscan uplift (Boiron et al., 2003; Vallance et al., 2004). Au deposits were formed by H_2O - CO_2 (± CH_4 and N_2) fluids in equilibrium with the metamorphic rocks and then diluted with surface fluids that have percolated during exhumation (Boiron et al., 2003).

In this study, we have analysed the compatible and incompatible metallic trace elements by LA-ICPMS in a series of basic and ultrabasic rocks from the Limousin thrust sheet of ophiolite-derived rocks, and from a series of granites as well as in the mineral assemblage in the different host rocks. The main purpose consists of identifying the main hosts for the metallic trace elements and determining their behaviour and budget in non-mineralised rocks, in order to trace the source of trace elements transported by fluids involved in the Variscan ore deposits, at different scales.

2. Geological setting and studied samples

2.1. Limousin thrust sheet of ophiolite-derived rocks

The Limousin thrust sheet of ophiolite-derived rocks occurs as a 25 km long and 1–5 km wide belt of basic and ultrabasic rocks, segmented by Variscan and late Carboniferous faults. It belongs to the upper part of the Middle Allochthon and consists of remnants of an ancient oceanic crust (Santallier, 1981; Dubuisson et al., 1989; Berger et al., 2005, 2006) probably emplaced during the Cambro-ordovician rifting (Berger et al., 2010). Main lithologies are characteristic of a lherzolite-harzburgite ophiolite type and include diopside-bearing harzburgites, harzburgites, dunites, wehrlites, as well as troctolites, amphibolitic (meta)gabbros and basic dykes of mid-ocean ridge basalt affinity (Berger et al., 2005, 2006). The ultrabasic rocks are highly serpentinised (Dubuisson et al., 1989), with only rare relicts of olivine, spinel or pyroxene. Serpentinisation of ultrabasic rocks and amphibolitisation of the basic rocks result from intensive seafloor hydrothermal alteration under low-P conditions (~0.2 GPa) and decreasing temperature from high-T late-magmatic conditions to greenschist–zeolite metamorphic facies (Berger et al., 2005).

In this study, we have investigated the metallic trace element composition of a series of samples from La Flotte, Le Cluzeau and Saint-Laurent (St-Laurent) ophiolite-derived massifs (Fig. 2; Table 1): six serpentinites (LAU-1, LAU-2, CLUZ-6, FLOT-1, FLOT-4, FLOT2a and FLOT-2b) and four amphibolites (metamorphosed basic dykes CLUZ-1, CLUZ-1a; metagabbros CLUZ-4 and CLUZ-5) (El Korh et al., in press). Serpentinites from St-Laurent (LAU1, LAU2) display an assemblage of Mg-rich serpentine, chlorite forming veins, spinel, amphibole (composition from tremolite to Mg-hornblende) and rare relicts of olivine. These samples are comparable to the highly serpentinised dunites described by Dubuisson et al. (1989). Serpentinites from La Flotte (FLOT1, FLOT2a, FLOT2b) and Le Cluzeau (CLUZ6) contain serpentine that have partially to totally replaced olivine and pyroxene, as well as large lenses of chlorite + amphibole (tremolite to Mg-hornblende), spinel, iron oxides and sulphides (Figs. 3a–c). These samples may correspond to the serpentinised harzburgites or troctolites described by Dubuisson et al. (1989) and Berger et al. (2005). The major element composition of serpentinites is typical of ultrabasic rocks, with low SiO_2, TiO_2, Al_2O_3, Fe_2O_3, FeO, CaO, Na_2O and K_2O abundances, and a high MgO content. Serpentinites from La Flotte (FLOT1, FLOT2a, FLOT2b) and Le Cluzeau (CLUZ6) show slightly higher Al_2O_3, Fe_2O_3 and FeO abundances, and a lower XMg than samples from St-Laurent. Amphibolites (basic dykes CLUZ-1 and CLUZ-1a and metagabbros CLUZ-4 and CLUZ-5) consist of green-brown amphibole (mainly Mg-hornblende), plagioclase, chlorite and iron oxides (Fig. 3d). Amphibole often shows evidence of alteration along grain rims and fractures. Amphibolites have a basic composition, with higher SiO_2, Al_2O_3, CaO and Na_2O contents and a lower MgO content than serpentinites (see also El Korh et al., in press).

2.2. UHP eclogite

Trace elements were also measured in one UHP zoisite-eclogite (sample L04-143; from Berger et al., 2010). It crops out 500 m away from the St-Laurent ophiolite-derived massif, in contact with a leucogratic orthogneiss lens (UGU), within the LGU. Formation of the magmatic precursors of UHP eclogites in the Limousin has been dated between 489 and 475 Ma (U–Pb; zircon) (Berger et al., 2010). Peak pressure and temperature conditions have been estimated to be 660°C and 2.9 GPa and occurred at c. 412 ± 5 Ma (U–Pb age; zircon), i.e. earlier than the middle Devonian continent-continent collision (Berger et al., 2010). The studied zoisite-eclogite L04-143 is composed of garnet, zoisite, omphacite, and rutile. Partial retrogression is evidenced by the formation of amphibole around omphacite and zoisite and ilmenite rimming rutile (for the detailed description of the sample, see Berger et al., 2010).

2.3. Granites and gneiss

We have also examined the mineral trace element composition in a series of granites and gneiss from the Vaulry (leucogranites VAU2 and VAU6; Vallance et al., 2001) W–Sn metallic district, from the Saint-Yrieix (St-Yrieix) Au district (St-Yrieix: orthogneiss GNEISS-SY-1; Lauriéras: leucogranite Lau10e, Essarraj et al., 2001; Cheni: leucogranite Che10b, Vallance et al., 2004), and from the Saint-Sylvestre (St-Sylvestre) (IGAR744, 820A; El Jarray, 1993) and La Marche (Ay.MAR; Ayt Ougougdal, 1994) leucogranites (U districts) (Figs. 3e and f).

2.3.1. Vaulry W-Sn district

The Vaulry W-Sn district is hosted by the Blond RMG pluton (Cuney et al., 1994; Raimbault, 1998; Le Carlier de Veslud et al., 2000; Vallance et al., 2001; Alexandrov et al., 2002). It constitutes a late generation of peraluminous granites in the North-western part of the FMC (Améglio et al., 1998). The Blond granite forms a 17 km long and 5 km wide, E–W elongated pluton, which is located at 30 km west of Limoges (France) (Chèvremont et al., 1992). The age of magmatic emplacement is estimated to be c. 313 Ma, i.e. during the late stages of the Variscan magmatism (^{40}Ar/^{39}Ar age on muscovite; Alexandrov et al., 2002). Intrusion of the Blond granite results from the activity of the Oradour strike-slip fault, which is interpreted as the root of the granite, along the SW boundary of the pluton (Soufi, 1988; Améglio et al., 1998). To the North, the Blond granite intruded into the UGU, while to the south it intruded into the late Devonian Cieux-Vaulry and Glane biotite-rich granites, which were emplaced into the LGU (Soufi, 1988; Améglio et al., 1998; Vallance et al., 2001). Thus, it is suggested that the Blond pluton is located at the boundary between the UGU and the LGU (Vallance et al., 2001). The studied granites (VAU2 and VAU6) are mainly composed of quartz, K-feldspar partially sericitised, plagioclase, biotite and muscovite, and contain zircon inclusions in biotite (Fig. 3e).

W-Sn deposits are mainly located along the eastern boundary of the Blond pluton and result from fluid percolation in the northern border of the Blond pluton (Le Carlier de Veslud et al., 2000; Vallance et al., 2001). They were interpreted to be synchronous to the rare metal leucogranite emplacement (Alexandrov et al., 2000; Cuney et al., 2002). However, a recent study has dated wolframite crystallisation (W ore) at 298.0 ± 1.2 Ma (U–Pb age) (Harlaux et al., 2018). W-Sn mineralisations are hosted by subvertical quartz veins, locally with muscovite and minor quartz selvages on the Vaulry area. W-Sn were deposited by a mostly aqueous fluid, with moderate salinity and minor volatile component, at 315°C under hydrostatic to suprahydrostatic pressures corresponding to a depth of c. 5.5 km (Vallance et al., 2001). The mineralising fluid result from the mixing of different types of fluids: 1) the early high-temperature (430°C) saline fluid responsible for granite muscovitisation, 2) a high-temperature (310–350°C) and moderately saline fluid with a diluted volatile component, 2) a low-temperature (230°C) and low-salinity evolved meteoric fluid (Vallance et al., 2001).

2.3.2. St-Yrieix Au district

The St-Yrieix district is a major gold district located in the North-western part of the FMC (e.g. Essarraj et al., 2001, Boiron et al., 2003; Vallance et al., 2004). It consists of orthogneisses and micaschists of the Lower Gneiss Unit, with amphibolite or leptynite intercalations. During the Neo-Variscan period, a limited granitic magmatism intruded the LGU and resulted in several granite km-large stocks: Le Bourneix, Le Chalard and Chadefaine bodies consisting of the biggest stocks (Stussi and La Roche 1984; Calli, 1988; Bouchot et al., 1989; Pastier 1992; Chalier, 1993; Marignac and Cuney, 1999). The granite stocks and their crosscutting aplo-pegmatite dykes were dated at 338.5 ± 1.5 Ma (^{40}Ar/^{39}Ar method; Alexandrov, 2000). Besides, outcropping basic lamprophyre dykes were dated at 290 ± 5 Ma (Rb/Sr; Chalier et al., 1994) and are probably related to the extensional tectonics during the Stephanian-Permian (Vallance et al., 2004).

Au deposits were formed in long-lived ductile fault zones c. 310–295 Ma ago (Bouchot et al., 1989, 1997; Marignac and Cuney, 1999; Le Carlier de Veslud et al., 2000). They were emplaced under P–T conditions of 350–400°C and 100–200 MPa, to surface conditions and recorded a pressure drop from lithostatic to hydrostatic conditions (e.g. Boiron et al., 1990; Marignac and Cuney, 1999, Boiron et al., 2003). Au was deposited mainly as free gold and at a lesser degree as gold-rich arsenopyrites by H_2O – (CO_2 ± CH_4 and N_2) fluids in equilibrium with the metamorphic rocks mixing with low-salinity surface water of meteoric origin percolating the basement rocks at low temperatures (150–250°C) under hydrostatic pressure conditions (Cathelineau et al., 1993, Essarraj et al., 2001, Boiron et al., 2003).

The studied granites and orthogneiss are composed of quartz, K-feldspar (including microcline), plagioclase (albite), biotite and muscovite. Biotite is partially altered in chlorite in sample Che10b. Accessory minerals consist of apatite and zircon inclusions in biotite crystals (Table 1). Muscovite is absent from sample LAU10e (Table 1), which also contain accessory pyrite and Fe-Ti oxides. K-feldspars are often altered in sericite. Hydrothermal alteration is also evidenced by the formation of fine Fe hydroxides/clay in association with sericite.

2.3.3. St-Sylvestre–Western Marche complex

The St-Sylvestre–Western Marche two-mica peraluminous leucogranites host large U deposits in the Western FMC (e.g. Cuney et al., 1990; Cathelineau et al., 1990; Marignac and Cuney, 1999). The leucogranitic complex consists of a 2–3 km thick laccolith of 6 km deep roots maximum, emplaced at a depth of 10.5 ± 1.5 km (Scaillet et al., 1996a). The magmatic emplacement has been dated at 324 ± 4 Ma (U–Pb ages on zircon and monazite) (Holliger et al., 1986), i.e. during the Early Carboniferous syn- to late-collision exhumation (Le Carlier de Veslud et al., 2013). Younger $^{40}Ar/^{39}Ar$ ages from 315 Ma to 300 Ma towards the base of the complex reflect a second exhumation stage, responsible for the uplift of the St-Sylvestre complex by unroofing of the overlying metamorphic and granitoidic formations during the late-orogenic Variscan extension (Scaillet et al., 1996a, 1996b; Le Carlier de Veslud et al., 2013). Intensive deformation associated with fluid migration during exhumation of the ductile crust was dated at 294 ± 19 Ma (Rb-Sr isochron age) (Luais et al., 2009). U enrichment in the peraluminous granites results from multi-stage magmatic processes (partial melting and granite intrusion) followed by hydrothermal remobilisation (Cuney et al., 1990). The formation of the main hydrothermal U deposits was dated at 280 Ma (U–Pb age) (Cathelineau et al., 1990). Outside the mineralised zones, three types of fluids have percolated into the St-Sylvestre granitic complex during the late stages of the Variscan orogeny: 1) high-T aqueous-carbonic fluids, 2) lower-T aqueous fluids probably related to the granite episyenitisation, and 3) low-T temperature aqueous fluids (El Jarray et al, 1994; André et al., 1999). Minor W and Sn mineralisation are also hosted by the St-Sylvestre granites, and are located along the granite/metamorphic rock contact (Cuney et al., 1990). The presence of both major U and minor W–Sn ore deposits result from different metal fractionation stages related to the different Variscan magmatic stages (Cuney et al., 1990).

While this study does not consider U sources, granites from St-Sylvestre and La Marche were analysed to determine if they may be potential source of minor deposits. The studied granite samples from La Marche (Ay.MAR) and St-Sylvestre (820A, IGAR744) are composed of quartz, K-feldspar, plagioclase, biotite and muscovite (Fig. 3f). Accessory minerals consist of apatite as well as zircon and monazite inclusions in biotite crystals (Table 1). K-feldspar and plagioclase have undergone partial sericitic alteration.

3. Analytical techniques

3.1. Whole rock trace element composition

The whole rock trace element concentrations were analysed at the SARM (CRPG-Nancy) by inductively coupled plasma mass spectrometry (ICPMS), using a ThermoFisher X7 spectrometer (ThermoFisher Scientific, Germany and USA). 200 mg of powdered samples were fused with 600 mg $LiBO_2$ at 980°C, and dissolved in a mixture of HNO_3 (5%), H_2O_2 (0.5%) and glycerol (10%) prior to analysis, according to the procedure described by Carignan et al. (2001). Uncertainties are generally <8% at 1σ.

3.2. Major element composition of minerals

Major element compositions of minerals were analysed by wavelength-dispersive analysis using a five-spectrometer CAMECA SX100 electron microprobe at the Service Commun de Microscopie Electronique et Microanalyses (SCMEM, GeoRessources). The accelerating voltage and the beam current were 15 kV and 12 nA, respectively. Counting times were 10 s. The beam size was set to 1 µm. Si, Al, Mg and Na were analysed on a TAP crystal. Fe and Mn were run on a LIF crystal, Ca and Cr on a PET crystal. K, Ti and Cl were measured with a LPET crystal. Raw data were reduced using the X-PHI quantification procedure (Merlet, 1994). All iron was calculated as Fe^{2+} in chlorite, olivine, phengite and feldspaths. Fe^{2+} and Fe^{3+} in amphibole and serpentine, as well as water contents (chlorite, micas, amphibole, serpentine), were calculated assuming ideal stoichiometry. Representative major element compositions of minerals in the studied basic and ultrabasic samples and gneiss GNEISS-SY-1 are given in the Supplementary Table S1.

3.3. Trace element composition of minerals

Trace element abundances in minerals were analysed by laser-ablation inductively-coupled plasma mass spectrometry (LA-ICPMS) at GeoRessources. Analyses were carried out using an Agilent 7500c quadrupole spectrometer interfaced to a GeoLas Pro 193 nm ArF excimer laser ablation system (Lambda Physik, Germany). Operating conditions consisted of a 5 Hz repetition rate, a ~ 10 J/cm^2 fluence, and a 44 μm beam size. Helium was used as the carrier gas (0.8 L/min) and was mixed with Ar prior to its introduction in the plasma (1.5 L/min). Peak hopping mode was employed, as well as dual (counting and analogue) secondary electron multiplier (SEM) detector mode. Analytical list included the following isotopes: ^{27}Al, ^{29}Si, ^{42}Ca, ^{49}Ti, ^{45}Sc, ^{51}V, ^{53}Cr, ^{55}Mn, ^{57}Fe, ^{59}Co, ^{60}Ni, ^{63}Cu, ^{66}Zn, ^{69}Ga, ^{74}Ge, ^{75}As, ^{95}Mo, ^{107}Ag, ^{118}Sn, ^{121}Sb, ^{182}W, ^{197}Au, ^{208}Pb, ^{209}Bi. Dwell times were 10 ms for major elements and 20 ms for the trace elements. The ThO$^+$/Th$^+$ and Ca^{2+}/Ca$^+$ ratios were carefully optimised to about 0.2–0.7 and 0.3–0.5% respectively, by ablation of the National Institute of Standards and Technology standard reference material SRM 610, a synthetic glass doped with trace elements. The low oxide and doubly charged ion production rates prevented polyatomic and doubly charge ion interferences. Acquisition times for background and ablation signals were 60 and 40 s, respectively, allowing the measurement of duplicate spots per analysis.

The NIST 610 reference material was used for external standardisation, using the preferred values of average element abundances from the GeoRem database (Max Planck Institut für Chemie, Mainz, Germany; http://georem.mpch-mainz.gwdg.de). Typical analytical series consisted of 10–16 measurements of mineral samples, bracketed at the start and end of each analytical sequence by 2 measurements of the primary standard. Intensity vs. time data were reduced using the ratio-of-the-mean intensities method in an Excel spreadsheet, following the procedure defined in Longerich et al. (1996). Internal standards were ^{29}Si (amphibole, serpentine, plagioclase, olivine, chlorite, garnet, omphacite, quartz, biotite, muscovite), ^{57}Fe (Fe oxides and sulfides), ^{27}Al or ^{53}Cr (spinel) and ^{49}Ti (rutile), based on the mineral major element compositions determined by microprobe analysis. During data treatment, intervals of 45 and 25 s were selected for the background and the ablation signal, respectively, with an offset of 3 s from the beginning of the ablation to avoid unstable parts of the signal, resulting from large particle production and/or surface contamination. No correction for down-hole fractionation was applied. The instrumental mass bias was corrected using a linear regression function, considering an equal time interval between each analysis. The minimum detection limit, corresponding to three times the standard deviation of the background measurement, is based on the 99% confidence level over the Gaussian counting statistics. Limits of detection are generally 0.1–5 ppm for V, Co, Ga, Ge, Mo, Ag, Sn, Sb, W, Au, Pb and Bi, 1.2–20 ppm for Cu, Zn and As, 1.5–50 ppm for Cr, Ni and Ti. Uncertainties on individual measurements at 1σ are 1.1-15%, and up to 30% for elements, whose abundance is <0.5 ppm. The NIST SRM 612 glass was employed as secondary standard and yielded trace element abundances in agreement with the reference values (see Supplementary Table S2).

4. Results

4.1. Serpentinites

4.1.1. Bulk rocks

Serpentinites display high Cr, Co and Ni abundances (2436–3427, 87–137 and 1326–1992 ppm, respectively), and to a lesser extent, high V and Zn concentrations (36–64 and 44–81 ppm, respectively) (Table 2; Figs. 4 and 5). The compatible and incompatible trace element concentrations in serpentinites are generally typical of the Primitive Mantle (PM; "pyrolite" in McDonough and Sun, 2005) (Table 2). The studied serpentinites harzburgites have a $(Ce/Yb)_{PM}$

ratio of 0.40 to 0.70, while the light REE (LREE) abundances are below detection limit in serpentinites from St-Laurent LAU1 and LAU2. In a PM-normalised multi-element diagram, serpentinites show a flat pattern for medium rare earth elements (MREE) and heavy REE (HREE). Serpentinites LAU1 and LAU2 are depleted in MREE compared to HREE. Th, U, High Field Strength Element abundances (HFSE) are relatively variable: Th, U, Nb and Ta abundances are below detection limit in all serpentinites, while Zr, Hf and Ti are only measured in the serpentinites from La Flotte and Le Cluzeau (Fig. 4a). Ti and Cu are abundant in serpentinites FLOT2a, FLOT2b and CLUZ6 (378–731 and 119–326 ppm, respectively), while they are generally below detection limit in serpentinites LAU1 and LAU2. However, Ti is depleted and Cu is strongly enriched in the serpentinites compared to the Primitive Mantle (Table 2; Fig. 4b). Ga and Ge abundances in serpentinites FLOT2a, FLOT2b and CLUZ6 (3.7–4.3 and 0.89–1.2 ppm, respectively) are low but similar to the Primitive Mantle (4.0 ppm Ga and 1.1 ppm Ge). Lower Ga and Ge are measured in the serpentinites LAU1 and LAU2 (1.6–1.8 and 0.82–0.88 ppm, respectively). Mo, Ag, Sn, Au, Pb and Bi concentrations are generally below detection limit (Table 2). When detected, As, Sb, W contents in serpentinites are enriched compared to the Primitive Mantle.

4.1.2. Minerals

In serpentinites LAU1 and LAU2, serpentine is mostly magnesian, but its Mg# ratio decreases in altered zones (see also El Korh et al., in press). Serpentine in the serpentinites FLOT2a, FLOT2b and CLUZ6 is generally zoned in Fe_2O_3, FeO and MgO, and show a rimward increase of the Mg# (from 0.7 to 1.0). Relicts of olivine are dominated by the forsterite component (Mg# of 0.86–0.91). When present, chlorite and amphibole are magnesian. Spinel shows a large range of composition, with variable Al_2O_3, Cr_2O_3, Fe_2O_3, FeO, MgO contents.

Spinel is the main host for compatible trace metals (up to 0.1–1% Ti, V, Co, Ni, Cu and Zn; > 1% Cr). Cr, V and Ti abundances in chlorite and amphibole (Cr: 546–12280 ppm; V: 8.7–

188 ppm; Ti: 143–1808 ppm) are generally higher than in serpentine and olivine (Cr: 3.6–100 ppm; V: 0.53–8.6 ppm; Ti: 7.8–107 ppm) (Fig. 5), except for samples FLOT2a and LAU2 (Fe-rich generation), whose high concentrations in Cr, V and Ti (up to 221 ppm, 10209 ppm and 7360 ppm of Cr, V and Ti, respectively) may be related to small inclusions of spinel (Table 3). By contrast, serpentine and olivine display higher Co, Ni and Cu abundances (Co: 13–905 ppm; Ni: 479–6764 ppm; Cu: 1.3–1360 ppm) than amphibole and chlorite (Co: 26–108 ppm; Ni: 494–1481 ppm; Cu: 1.25–176 ppm). Zn, Ge and As concentrations are within the same range for serpentine, chlorite, amphibole and olivine (3.7–321, 0.33–5.1 and 1.3–31 ppm, respectively), while Ga is mainly hosted by amphibole (10–30 ppm), chlorite (1.2–20 ppm) and spinel (5.2–125 ppm) (Fig. 5; Table 3).

Serpentine generally shows low abundances of Sn, Sb, W and Pb (Sn and Sb < 1 ppm; Pb and W < 4 ppm), with the highest values being measured in the Fe-rich generation (up to 7.9 ppm W). Au, Mo, Ag and Bi are generally below detection limit, even if low concentrations of Mo, Ag and Bi may be detected in chlorite, serpentine or spinel.

Accessory Fe oxides and sulphides (pyrite) may have high and heterogeneous contents in compatible metals (up to 12263 ppm Cr, 2127 ppm Co, 79693 ppm Ni and 5508 ppm Cu), which may be related to small-size inclusions. However, their concentration in incompatible metals is generally low.

4.2. Basic rocks

4.2.1. Bulk rocks

Amphibolites show high bulk abundances of compatible metals (30 to 2000 ppm), with higher Sc, Ti and V contents, and lower Cr, Co, Ni and Zn contents than ultrabasic rocks. Cu abundances are lower than those of serpentinites from La Flotte and Le Cluzeau, but higher than those of serpentinites from St-Laurent. Amphibolites display REE abundances similar to the Primitive Mantle. In a PM-normalised multi-element diagram, amphibolites show a flat MREE and HREE pattern and LREE depletion, with a $(Ce/Yb)_{PM}$ ratio of 0.60 to 0.66, typical of normal mid-ocean ridge basalt (N-MORB) (Fig. 4a). Large Ion Lithophile Elements (LILE: Cs, Rb, Ba) and Sr abundances are slightly higher than N-MORB (Sun and Mc Donough, 1989) and Primitive Mantle. Two amphibolite samples show a positive Pb anomaly. The compatible and incompatible metal concentrations as well as the HFSE abundances are generally typical of N-MORB and ocean floor basalts (OFB; Jenner and O'Neill, 2002). Only Ti and Zn are depleted compared to mean OFB, while Cr shows a higher abundance (Table 2; Fig. 4b). Ga and Ge contents of amphibolite facies rocks (12–14 and 1.2–1.4 ppm, respectively) are higher than those of serpentinites. Ge content is typical of OFB (1.1–1.5 ppm; Jenner and O'Neill, 2012), but Ga content is slightly lower than in OFB (14–23 ppm; Jenner and O'Neill, 2012). Sn, Sb, W, Mo, Ag, Au and Bi abundances are generally below detection limit, though higher than mean OFB when measured (Table 2).

4.2.2. Minerals

In amphibolites, green-brown amphibole is mainly Mg-hornblende (see also El Korh et al., in press). Plagioclase composition varies from anorthite to labradorite in samples CLUZ1 and CLUZ4, and is mostly labradorite in samples CLUZ3 and CLUZ5. In amphibolite facies metagabbros and dykes, amphibole and accessory titanite are the main hosts for the compatible metals (24–1775 ppm of V, Cr, Ni; 1.4–93 ppm of Sc, Co, Cu, Zn). In amphibole, Ga, Ge and As abundances are relatively variable (2.3–17 ppm, 1.2–2.7 ppm and 1.3–8.8 ppm, respectively), while Sn and Sb contents are generally < 1 ppm (Table 4; Fig. 6). Titanite is the main host for Sn (4.7–5.6 ppm), W (16–18 ppm) and Ge (3.5–5.4 ppm). Accessory sulphides and oxides show high and heterogeneous concentrations in compatible and incompatible elements (up to 7180 ppm of Cr, 22078 ppm of Cr, 89963 ppm of Cu, and 99 ppm Ag). Plagioclase is the main host for Ga (10–21 ppm) and Pb (0.46–15 ppm), while it displays low abundances of other compatible and incompatible metals (Table 4).

4.3. UHP eclogite

4.3.1. Bulk rock

The zoisite-bearing eclogite have higher TiO_2, Al_2O_3, FeO contents and lower SiO_2, MgO and CaO contents than amphibolites. Eclogite L04-143 shows the highest Sc, Ti, V, Zn and Pb contents, although similar to those of OFB, and the lowest Cr, Co, Ni contents of the studied basic and ultrabasic rocks. Sn, Sb and Bi abundances are low but well measurable (≤ 0.5 ppm), while the W content is high (14 ppm) (Table 2). Ga and Ge are slightly higher than in amphibolite facies dykes (17 and 2.3 ppm, respectively) and metagabbros, although within the range of basic rocks (Ga: 8.7–23 ppm, Ge: 0.7–2.3 ppm; see El Korh et al., 2017 and references therein for a review).

4.3.2. Minerals

In the zoisite-eclogite, rutile and its ilmenite rims are the main host for Ti, V and Cr. Significant V and Cr amounts (56–986 ppm and 33–498 ppm, respectively) are also measured in the other minerals of the assemblage (omphacite, amphibole, zoisite, and, to a lesser extent, garnet) (Table 5; Fig. 7). Concentrations in Sc are relatively similar in all minerals (15–69 ppm). Sc, Co, Ni and Zn are abundant in all minerals. The highest Ni concentrations are measured in omphacite and retrograde amphibole, while Co is mainly enriched in amphibole and garnet (Fig. 7). Cu abundances are below 21 ppm in rutile, zoisite and amphibole. One measurement of omphacite has yielded a concentration of 89 ppm. Zoisite is the main host for Ga and Ge (111–186 and 8.8–19 ppm, respectively). Omphacite, garnet and retrograde amphibole are other important hosts for Ga and Ge (21–41 and 3.0–21 ppm, respectively). The incompatible metals are mainly concentrated into zoisite, rutile and retrograde amphibole (generally 1–20 ppm As, Mo, Bi, Sn, Sb and W). Rutile contains significant W abundances (up to 164 ppm). Pb abundances are also high in zoisite (75–98 ppm) and, to a lesser extent, in omphacite and amphibole (6.1–39 ppm) (Table 4).

4.4. Granites and gneisses

4.4.1. Bulk rock

The bulk rock major and trace element concentrations were measured in the gneiss GNEISS-SY-1. It is a high-SiO_2 orthogneiss, with high Al_2O_3 and K_2O contents and low FeO, Fe_2O_3 and CaO contents (Table 2). In a PM-normalised multi-element diagram (Fig. 4a), sample SY-GNEISS-1 display a pattern typical of the Upper Continental Crust (UCC), with Ti, Nb and Ta negative anomalies, Pb positive anomaly, and LREE > HREE [$(Ce/Yb)_{PM} = 4.0$]. Its Cs, V, Cr, Co and Ni contents are low (V: 17 ppm; Sc, Cr, Co, Ni < 5.6 ppm) compared to the UCC, as well as compared to the basic and ultrabasic rocks. Its Ti content is comparable to those of basic amphibolites. Ga and Ge contents (20 and 1.6 ppm, respectively) are comparable to those of UCC and granites (see El Korh et al., 2017 and references therein for a comparison) and slightly higher than those of basic amphibolites (Table 2). The gneiss GNEISS-SY-1 also shows higher Mo, Sn, Sb, W and Pb abundances than those of basic and ultrabasic rocks, but comparable to those of the UCC (Table 2; Fig. 4b).

4.4.2. Minerals

In granite and gneisses, the compatible and incompatible metals are mainly hosted by biotite and muscovite. Biotite (V: 3.1–447 ppm; Cr: 5.0–449 ppm; Co: 2.5–45 ppm; Ni: 3.0–98 ppm; Zn: 352–2902 ppm; Ti: 7976–21870 ppm) generally shows higher compatible metal abundances than muscovite (V: 1.4–153 ppm; Cr: 8.4–127 ppm; Co: 1.2–4.3 ppm; Ni: below detection limit; Zn: 12–466 ppm; Ti: 417–5036 ppm) (Fig. 8). The micas have variable contents in Sc (5.5–255 ppm) and Ga (61–282 ppm) and low contents in Ge, As, Sb, Pb and Bi (< 17 ppm). Cu (1.5–42 ppm) is mainly measured in biotite from Vaulry granites. Besides, micas display significant Sn and W contents (11–610 and 1.9–193 ppm, respectively), W being enriched in muscovite (2.0–193 ppm) compared to biotite (1.9–77 ppm) (Table 6).

Sn and W abundances significantly vary in biotite and muscovite between the different localities (Fig. 9). The highest Sn and W abundances are measured in Vaulry granites (VAU2 and VAU6), and decrease in the granites from La Marche (Ay.MAR), St-Sylvestre (820A and IGAR744) St-Yrieix (St-Yrieix: GNEISS-SY-1, Lauriéras: LAU10e, Cheni: Che10b) districts, which show the lowest Sn and W content. In the St-Yrieix district, biotite from gneiss GNEISS-SY-1 has higher W contents than biotite in granites Che10b and LAU10e, while biotite in sample Che10b shows higher Sn abundances. Zn and Ge abundances decrease from Vaulry to St-Yrieix granites in biotite and muscovite (Fig. 9; Table 6). On the other hand, Vaulry and St-Yrieix granites and gneisses have higher Sc contents than St-Sylvestre and La Marche granites. In the St-Yrieix district, Ni, Cr and V contents of biotite decrease from Lauriéras to St-Yrieix and Cheni (Fig. 9; Table 6). Samples from La Marche also show high V and Cr concentrations. By contrast, samples from the Vaulry district variable Cr and V contents from one sample to the other.

Au and Ag abundances are generally below detection limit in all minerals. Quartz, feldspars and apatite have low contents in compatible metals, and only show minor amounts of Sc, Ga, Ge, Sn and Pb, when detected. High Ti and W concentrations are also measured in accessory Fe-Ti oxides (sample LAU10e) (Table 6; Fig. 8).

5. Discussion

5.1. Trace element behaviour and mobilisation during high-T hydrothermal alteration in the Limousin ophiolite-derived rocks

5.1.1. Serpentinites

The major and trace element (including compatible elements, Ga, Ge, HFSE and REE) composition of serpentinites are generally typical of ultrabasic rocks and Primitive Mantle (Fig. 4a). During serpentinisation of peridotites and dunites, Sc, Ti, V, Cr, Co, Ni, Cu and Zn contained in olivine and spinel were mainly incorporated in chlorite, Fe-rich serpentine and Fe-poorer serpentine formed with decreasing temperature of alteration, as well as in the less abundant amphibole and accessory oxides and sulphides.

As, Ag, Sn, Sb, W, Pb and Bi are enriched in the serpentinites compared to the Primitive Mantle and mean OFB (Fig. 4b). It has been shown that As and Sb can be mobile and enriched in the oceanic crust during hydrothermal alteration (Spandler et al., 2004). Similarly, precipitation of oxides and sulphides during the early stages of hydrothermal alteration may be responsible for metal enrichment (e.g. Rouxel et al., 2003). As, Sn, Sb, Sn, Pb and Bi are distributed between all mineral phases, i.e. in olivine relicts, as well as in the newly-formed serpentine, chlorite, amphibole and oxides. Within each sample, higher metal concentrations are measured in the earlier Fe-serpentine generation, and decrease in the next Fe-poorer generation due to their lesser availability as hydrothermal alteration went along.

Two serpentinites (FLOT1, FLOT2a) contain olivine relicts. In both samples, Ag, Bi and Mo are only detected in serpentine and accessory sulphides and oxides. In sample FLOT1, Sn abundances are slightly higher in chlorite and amphibole than in olivine relicts and serpentine, while W is enriched in serpentine and amphibole compared to olivine. Sb abundances are similar in olivine relicts and in serpentine. Besides, As is enriched in olivine relicts compared to newly-formed minerals. In sample FLOT2a, both olivine relicts and serpentine contain As and Sn, with higher Sn concentrations measured in serpentine. W is mainly hosted by serpentine. The high As concentrations measured in olivine relicts and similar Sn abundances in olivine and serpentine may reflect: 1) Enrichment of the initial magmatic rock or, 2) Contamination of olivine through fracturation during serpentinisation. In other serpentinites (LAU2, FLOT2b, CLUZ6), serpentine is the main host for As, Ag, Mo, Sn, Sb, W and Bi, indicating that enrichment in incompatible metals results from the high-temperature hydrothermal alteration that have followed the formation of the oceanic crust (Berger et al., 2005, 2006).

5.1.2. Amphibolites

Amphibolite facies metagabbros and dykes display a major and trace element (including compatible elements, HFSE and REE) composition typical of N-MORB and OFB (Fig. 4a). Despite lower than those of OFB, Ga abundances are consistent with those of basaltic and gabbroic rocks (8.8–41; see El Korh et al., 2017 and references therein). Besides, enrichment in mobile LILE, Sr and Pb compared to N-MORB and PM results from seafloor hydrothermal alteration.

During amphibolitisation of gabbros and basic dykes, the transition metals (MgO, MnO, FeO, Sc, Ti, V, Cr, Co, Ni, Cu and Zn) were mainly incorporated into amphibole, titanite and accessory oxides and sulphides. Because of the strong affinity of Ga with Al (De Argollo and Schilling, 1978), Ga was preferentially incorporated into Al-rich plagioclase. Ca-plagioclase is also the main host for Pb. Titanite, a nesosilicate, is the main host for Ge, confirming the preferential incorporation of Ge in the less polymerised silicates (Bernstein, 1985; El Korh et al., 2017; Rouxel and Luais, 2017). During amphibolite facies metamorphism, Sn, Sb and W were preferentially into titanite and, to a lesser extent, into amphibole. Amphibole is the main host for As, while Ag and Bi are mostly hosted by sulphides and oxides. No relicts of primary assemblages being preserved, it is difficult to determine whether As, Ag, Sn, Sb, W and Bi enrichment is of magmatic or hydrothermal origin. However, by analogy with serpentinites, enrichment in As, Ag, Sn, Sb, W and Bi compared to OFB and PM is probably related to the high-temperature hydrothermal processes on seafloor.

5.1.3. UHP eclogite

The studied zoisite-eclogite L04-143, derives from an iron-rich plagioclase cumulate, which has probably been strongly metasomatised under UHP conditions (Berger et al., 2010). Its composition present characteristics of both UCC and ocean islan basalts (OIB), despite lower LILE, Th and U contents (Fig. 4a). For this reason, the initial setting of the magmatic protolith is difficult to be determined based on the trace element composition (continental intrusions or Fe–Ti oceanic gabbros) (Berger et al., 2010). While the major element composition of eclogite L04-143 – characterised by a low SiO_2 content and high TiO_2, Al_2O_3 and Fe contents – is different from those of amphibolites, its composition in compatible transition trace metals, Ga and Ge is similar to amphibolites and OFB, suggesting an oceanic affinity (Fig. 4b). By contrast, eclogite is enriched in As, Sb, W, Pb and Bi compared to PM and OFB, which may reflect either the primary magmatic composition, or enrichment during hydrothermal processes.

Most of the transition trace metals (Sc, Ti, V, Cr, Co, Zn) are distributed between all mineral phases, contrary to Cu, which is generally not measured in garnet and omphacite. Main UHP hosting minerals for Cu are zoisite and rutile. The high Cu abundance (89 ppm) measured in one omphacite crystal is probably related to a Cu-rich inclusion, such as rutile. Similarly, Ni is not detected in garnet and rutile, and was mostly hosted by omphacite and zoisite during the UHP stage. Partial retrogression of eclogite L04-143 was responsible for the transfer of a part of incompatible metals released by zoisite and omphacite to retrograde amphibole.

During UHP metamorphism, Ge was mainly incorporated into garnet and zoisite (an epidote-group mineral), as observed by El Korh et al. (2017) for HP rocks, while main hosts for Ga were Al-rich zoisite, omphacite and garnet. The incompatible metals As, Ag, Mo, Sn, Sb, W Pb and Bi were mainly distributed between rutile, zoisite, and, to a lesser extent, omphacite. During retrogression, Sn, Sb and W released by rutile and zoisite were incorporated into amphibole and ilmenite, while Ga, Ge, As, Mo, Pb and Bi were only incorporated into retrograde amphibole.

5.2. Trace element partitioning in gneiss and granites

Orthogneiss GNEISS-SY-1 from the St-Yrieix district belongs to the Lower Gneiss Unit (Lower Allochthon). Its major element, LILE, HFSE and REE compositions are typical of granitic rocks from the Upper Continental Crust. Trace element compositions of the mineral assemblage show that micas (biotite and muscovite) are the main hosts for the transition metals, as well as for Ga, Ge, As, Ag, Sn, Sb, W and Pb. Because of the importance of micas in the incompatible metal budget for gneiss GNEISS-SY-1, focus has been placed on biotite and muscovite in the granite samples to discuss the provenance of the metallic pre-concentration.

In a previous study, Wolf et al. (2018) have highlighted the importance of muscovite and biotite in trace element partitioning in migmatites during melting. In particular, Sn remains into the restite and becomes depleted in the melt as long as micas are stable in the restite during partial melting. Feldspaths (microcline and albite) are the main hosts for Pb and contain high Ga abundances, as well as low Sc, Ge and Sn contents. However, it is difficult to attribute measured concentrations to pristine magmatic contribution, or if they were modified by hydrothermal processes related to metamorphism. Trace element compositions of micas within each sample are relatively homogeneous, while they vary significantly according to the locality. The geographical variation is particularly evident for Sn and W as well as for Zn, Ge and Cu, whose abundance generally decrease from Vaulry to La Marche, St-Sylvestre and St-Yrieix. The V and Cr abundances in biotite also vary from one locality to the other. In the St-Yrieix district, the V and Cr abundances increase as the distance to the ophiolite-derived rocks decreases, suggesting a local source for Cr and V.

5.3. Tracing the sources of metallic pre-concentrations in North-western Limousin

5.3.1. Gold

Mineralised Au-bearing quartz veins in the Limousin area are mostly hosted in the Lower Allochthon (Lower Gneiss Unit). However, the sources of Au in the Variscan belt are not known precisely and were suggested to derive from the structurally overlying Upper Gneiss Unit (Marignac and Cuney, 1999). Different sources were considered for the Limousin Au deposits: Proterozoic volcano-sedimentary rocks (Braux et al., 1991); Cambro-ordovician clastic rocks (Leblanc, 1989) or amphibolites and ultrabasic rocks from the LAGs (Floc'h et al., 1984). Based on Pb isotope analyses, Marcoux and Bonnemaison (1988) have suggested a mantle origin for Au. During this study, Au abundances were below detection limit (0.1–1 ppm) in minerals from ultrabasic and basic rocks of the Limousin ophiolite-derived rocks (Upper Gneiss Unit). Our data do not allow determining any source for Au in the ultrabasic and basic rocks of the Limousin thrust sheet of ophiolite-derived rocks.

The Lower Gneiss Unit is considered as possible sources for Au deposits in the St-Yrieix district (Cuney et al., 1990). However, the measured Au abundances were below detection limit in the mineral assemblage of gneiss GNEISS-SY-1 (Lower Gneiss Unit). Further systematic studies on accessory minerals from the lower gneiss unit are needed to trace the source of Au. In addition, based on our results, the granitic rocks are not the direct sources for Au, but served as heat source for the circulation of Au-mineralising hydrothermal fluids in faults adjacent to granites (Boiron et al., 2003).

5.3.2. Tungsten and tin

In the North-western Limousin, the Blond leucogranite (Vaulry district) hosts major W-Sn deposits, while contemporaneous leucogranites from the St-Sylvestre–Western Marche U district also contains minor W-Sn (Fig. 10). Different sources were regarded for W and Sn ore deposits in the FMC (Marignac and Cuney, 1999). While crustal or mantellic sources (granites and LAG) have been discussed, mobilisation of W and Sn is thought to be the result of the percolation of fluids of metamorphic origin (Caron, 1994; Vallance et al., 2001). In the Montagne Noire and Cévennes (southern FMC), metapelites were considered as the primary source of W, which was remobilised during hydrothermal processes related to subsequent LP–HT metamorphism (Gibert et al., 1988, 1992). More recently, the relationship between granites and W–Sn ore deposits has been pointed up: granites are thought to represent either the direct metal source or the thermal source that has driven hydrothermal circulation of mineralising fluids (Vallance et al., 2001;

Harlaux et al., 2018). Pb isotopes has allowed the determination of different sources for W-Sn deposits according to their emplacement: 1) deposits in Palaeozoic rocks derive from sedimentary, granitic and metamorphic rocks from old cratonic areas, i.e. from recycled Gondwanian crust; 2) deposits in Devonian rocks derive from more juvenile material (Harlaux et al., 2018).

In the North-western Limousin, amphibolites from the St-Yrieix district (LAG; UGU) display relatively high W and Sn contents (1–17 ppm and 5–24 ppm, respectively; Calli, 1988). W and Sn enrichment may have been caused by the same hydrothermal processes that have altered the amphibolites and triggered Au, As, Co and V enrichment (Calli, 1988). By contrast, serpentinites and amphibolites from the Limousin thrust sheet of ophiolite-derived rocks are characterised by low Sn and W abundances in whole rocks and minerals. Despite intensive fluid-rock interaction, the high-T hydrothermal alteration responsible for serpentinisation and amphibolitisation that have followed magmatic emplacement was not responsible for any significant W and Sn pre-concentration. Moreover, these hydrothermal processes cannot be responsible for W and Sn transport to the mineralised veins, because they occurred after the formation of the magmatic precursors of serpentinites and amphibolites, i.e. c. 100 Ma earlier than the mineralisation age (Berger et al., 2010; Harlaux et al., 2018). For this reason, the Limousin thrust sheet of ophiolite-derived rocks, deriving from a mantle source (such as a mid-ocean ridge–lherzolite-harzburgite ophiolite type; Berger et al., 2006), cannot be considered as an effective source for W and Sn mineralisation.

Because of metamorphic hydrothermal processes that have affected the UHP zoisite-eclogite (Berger et al., 2010), it is difficult to decipher whether the high W and Sn concentrations (compared to the Primitive Mantle) reflect the pre-UHP signature of its magmatic protolith, or metasomatic overprint. Fluid-rock interactions are thought to have occurred during the peak metamorphic UHP stage, i.e. at c. 412 ± 5 Ma, by interaction with a fluid released by the dehydrating sediments during subduction (Berger et al., 2010). However, W–Sn mineralisation are younger, with late Variscan ages (333–298 Ma; Harlaux et al., 2018). Thus, even if W (and Sn) enrichment in the UHP zoisite-eclogite results from fluid-rock interactions, it cannot be related to the same hydrothermal event that was responsible for W–Sn major and minor deposits. For the same reason, the dehydrating UHP eclogite cannot be regarded as a source for W- and Sn-transporting fluids.

In gneiss and granites, variations in the trace element composition of micas show a clear geographical correlation with the different districts (Figs. 9 and 10). Biotite and muscovite in leucogranitic samples from the Vaulry W–Sn major district display the highest W and Sn concentrations. Micas in the leucogranites from La Marche (Ay.MAR) and St-Sylvestre (820A and IGAR744), which host minor W–Sn deposits have lower W and Sn concentrations than those of Vaulry. The lowest Sn concentrations are measured in micas from the gneiss and granites from the St-Yrieix Au district (St-Yrieix, Cheni, Lauriéras), which are located farther from the Vaulry district (Fig. 10). Muscovite in sample GNEISS-SY-1 displays variable W and Sn concentrations. However, biotite in gneiss GNEISS-SY-1 has W abundances within the same range as biotite in leucogranite IGAR744 (St-Sylvestre) and higher W abundances than biotite in leucogranite 820A (St-Sylvestre). Our data for biotite and muscovite confirm the geographical correlation shown by previous results obtained for whole rocks: granites from Le Bourneix (St-Yrieix) have lower Sn concentrations (5–18 ppm, up to 61 ppm in an altered granite; Calli, 1988) than granites from La Marche (15–49 ppm, up to 79 ppm in aplites; Ayt Ougougdal, 1994), and from Blond-Vaulry granites (212–709 ppm, Belksami, 1993), rhyolites (450–503 ppm; Belksami, 1993) and microgranite dykes (18–191 ppm; Ebougué, 1995). Similarly, low W abundances were measured in granites from Le Bourneix (St-Yrieix) (1–7 ppm; Calli, 1988). W abundances increase in microgranites (5–18 ppm; Ebougué, 1995), granites (11–12 ppm; Belksami, 1993) and rhyolites (22–71 ppm; Belksami, 1993) from the Blond–Vaulry area.

According to Romer and Kroner (2015, 2016), Sn and W mineralisations in Palaeozoic basements of the western and central Variscan belt are related to the closure of the Rheic ocean. They propose that enrichment of Sn and W in granites results from three processes: 1) weathering-related enrichment in Sn and W of Cadomian sediments, 2) redeposition and accumulation of the sediments during tectonic processes and, 3) melting of the Sn–W-rich sedimentary rocks. Wolf et al. (2018) have demonstrated the role of the melting temperature and the protolith composition of migmatite for Sn partitioning between granitic melt and minerals from the restite. The authors explain metal enrichment in granite bound Sn mineralisation as the result of multiple extraction of Sn-depleted melt at low-temperature, while Sn remains trapped in micas from restite parts during partial melting. While the low-temperature Sn-depleted melts are expected to be released and lost, late granititic melts formed at high-temperature during the breakdown of Sn-rich restite become enriched in Sn, contrary to Cr, V and Ni, which remain in the restite (Wolf et al., 2018). In the same way, our results indicate that the geographical variation in Sn and W composition, as well as in Cr, Ni, V, Ge, Zn and Cu observed between the Limousin districts (Figs. 9 and 10) could be the result of variable source composition of sedimentary protoliths, variable anatexis degrees or late- to post-magmatic processes.

Differences in W and Sn within the rocks from the St-Yrieix district may reflect local enrichment of W and Sn resulting from variations in the nature of the rock or from variations in the geodynamic setting: biotite from orthogneiss GNEISS-SY-1, i.e. from the Lower Gneiss Unit, has higher W contents than biotite in the late-Variscan leucogranites Che10b and LAU10e. Besides, biotite in the leucogranite Che10b shows higher Sn abundances than the gneiss. The lithological and structural control on W and Sn concentrations within the St-Yrieix district is also evidenced by previous data obtained from a series of granites, paragneiss, cataclastic/brecciated quartzo-feldspathic rocks, argilo-siliceous cataclasites and auriferous quartz breccias from the Cros Gallet Au mine from Le Bourneix (Calli, 1988). W abundances are low in granites (1–3 ppm) and increase in the quartzo-feldspathic rocks (2–7 ppm), which correspond to altered and deformed granites (Calli, 1988). Besides, Sn abundances of 5–18 ppm were measured in paragneiss, granites, cataclastic/brecciated quartzo-feldspathic rocks and argilo-siliceous cataclasites. Higher values were obtained in altered granites and quartz breccias (up to 118 ppm; Calli, 1988). Our results for the different districts argue for a local source of W and Sn pre-concentrations, in agreement with Vallance et al. (2001), who has considered the Blond granite as the main source for W–Sn mineralisation in the Vaulry major district. Subsequent percolation of hot pseudo-metamorphic fluids in the Blond granite has probably leached W and Sn, and allowed precipitation of W- and Sn-rich minerals (wolframite, scheelite, cassiterite) in hydrothermal veins (Vallance et al., 2001). By analogy, the St-Sylvestre and La Marche leucogranites may be the local source for the minor W–Sn occurrences hosted in the two districts.

6. Conclusions

LA-ICPMS analyses of the main rock-forming minerals of granites, amphibolites and serpentinites have allowed acquiring new in-situ data to trace metal sources within the different lithologies of the Limousin. Serpentinites from the Limousin ophiolite-derived rocks have compatible and incompatible trace element compositions typical of the Primitive Mantle, with high concentrations in compatible transition metals (Sc, V, Cr, Co, Ni, Zn, Cu) and low abundances of incompatible metals (Ge, Ga, Mo, Sn, Sb, W). Associated amphibolites deriving from gabbros and basic dykes display trace element compositions typical of N-MORB and OFB, with high abundances in compatible metals and low contents in incompatible metals. Both ultrabasic and basic rocks show enrichments in As, Ag, Sn, Sb, W, Pb and Bi compared to PM and OFB, which may reflect either a protolith enriched in incompatible metals, or the fingerprints of high-temperature to low-temperature hydrothermal alteration that have followed the oceanic crust emplacement. Besides, the UHP zoisite-eclogite is generally richer in compatible and incompatible trace elements than other ultrabasic and basic rocks, with the exception of Cr, Co and Ni. The origin of incompatible metals (including As, Sb, W, Pb and Bi) is uncertain, and may reflect enrichment of the magmatic protolith (i.e. a Fe-rich plagioclase cumulate; Berger et al.,

2010) or enrichment during metasomatic processes related to the UHP metamorphic stage. However, the different hydrothermal processes that have affected the Limousin ophiolite-derived rocks and UHP eclogite are not contemporaneous with the formation of the mineralised veins, such as Au or W–Sn deposits. Thus, despite their proximity with the Au deposits, serpentinites, amphibolites and UHP eclogites do not appear to have play a role in the formation of Au deposits.

In all the studied granites and gneiss, the metallic trace elements are mainly hosted by accessory sulphides and oxides, as well as by biotite and muscovite, which contain significant Sn and W contents, low amounts of Ge, As, Sb, Bi and variable amounts of Sc, Cu and Ga. Quartz and feldspars only show minor amounts of Sc, Ga, Ge, Sn and Pb. Variations in W and Sn abundances in micas allow tracing the pre-mineralisation W and Sn concentrations in the different granite-hosted ore districts. Leucogranites from the Vaulry major W–Sn ore deposit display the highest W and Sn concentrations. W and Sn abundances decrease in the leucogranites from La Marche and St-Sylvestre U districts, which host minor W–Sn deposits. The smallest concentrations are generally measured in micas from the orthogneiss and leucogranites from the St-Yrieix Au district (St-Yrieix, Cheni, Lauriéras). In agreement with previous studies, our results argue for a local source of W and Sn and highlight a geographical correlation between W and Sn concentrations in the mineral assemblage of granites and W–Sn ore deposits.

7. Acknowledgments

Thanks to Chantal Peiffert for technical assistance in the LA-ICPMS laboratory, to Delphine Yeghicheyan (SARM, CRPG-CNRS, Nancy) for contribution to whole rock analyses, and to Olivier Rouer for help in the microprobe laboratory. We thank Julien Berger for sending UHP zoisite-eclogite sample L04-143. This study benefited from the detailed reviews of Michel Faure and an anonymous reviewer. We thank Xian-Hua Li for the editorial handling of our manuscript.

The research was supported by project P300P2_147749 of the Swiss National Science Foundation, as well as by the French National Research Agency through the national program "Investissements d'avenir" (ANR-10-LABX-21–LABEX RESSOURCES21). This is CRPG contribution n°2725.

8. Electronic Appendix: Supplementary Tables are associated with this article.

9. References

Alexandrov, P., 2000. Géochronologie U–Pb et 40Ar/39Ar de deux segments de la chaîne Varisque: le Haut Limousin et les Pyrénées Orientales. Unpublished PhD thesis, INPL, Nancy, France, 186 pp.

Alexandrov, P., Cheilletz, A., Deloule, E., Cuney, M., 2000. 319 ± 7 Ma age for the Blond granite (northwest Limousin, French Massif Central) obtained by U/Pb ion-probe dating of zircons. Comptes Rendus de l'Académie des Sciences, Paris 330, 1–7.

Améglio, L., Vigneresse, J.L., Bouchez, J.L., 1997. Granite pluton geometry and emplacement mode inferred from combined fabric and gravity data. In: Bouchez, J.L., Hutton, D.H.W., Stephens, W.E. (Eds.), Granite: From Segregation of Melt to Emplacement Fabrics. Kluwer Academic Publishers, Dordrecht, Boston, London, pp. 199–214.

André, A.S., Lespinasse, M., Cathelineau, M., Boiron, M.C., Cuney, M., Leroy, J., 1999. Late hercynian fluid percolation in the Saint- Sylvestre granite (NW French Massif central): Fluid inclusion data on the Razès-Saint Pardoux area. Comptes Rendus de l'Académie des Sciences, Paris 329, 23–30.

Arthaud, F., 1970. Étude tectonique et microtectonique comparée de deux domaines hercyniens: les nappes de la Montagne Noire (France) et l’anticlinorium de l’Iglesiente (Sardaigne). Thèse d’État, Université de Montpellier (France),175 p.

Arthaud, F., Matte, P., 1975. Les décrochements tardi-hercyniens du sud-ouest de l'Europe. Géométrie et essai de reconstitution des conditions de la déformation. Tectonophysics 25, 139–171.

Ayt Ougougdal, M. 1994. Contrôles magmatiques, structuraux et hydrothermaux de la formation des épisyénites de la Marche occidentale. Unpublished PhD Thesis, INPL, Nancy, France, 245 pp.

Belksami, M., 1993. Pétrographie et géochimie des granites à métaux rares. Unpublished PhD Thesis, INPL, Nancy, France, 588 pp.

Bernstein, L.R., 1985. Germanium geochemistry and mineralogy. Geochimica et Cosmochimica Acta 49, 2409–2422.

Berger, J., Féménias, O., Mercier, J.C.C., Demaiffe, D., 2005. Ocean-floor hydrothermal metamorphism in the Limousin ophiolites (western French Massif Central): evidence of a rare preserved Variscan oceanic marker. Journal of Metamorphic Geology 23, 795–812.

Berger, J., Féménias, O., Mercier, J.C.C., Demaiffe, D., 2006. A Variscan slow-spreading ridge (MOR-LHOT) in Limousin (French Massif Central): magmatic evolution and tectonic setting inferred from mineral chemistry. Mineralogical Magazine 70, 175–185.

Berger, J., Féménias, O., Ohnenstetter, D., Bruguier, O., Plissart, G., Mercier, J.-C.C., Demaiffe, D., 2010. New occurrence of UHP eclogites in Limousin (French Massif Central): Age, tectonic setting and fluid–rock interactions. Lithos 118, 365–382.

Boiron, M.-C., Cathelineau, M., Banks, D.A., Fourcade, S., Vallance, J., 2003. Mixing of metamorphic and surficial fluids during the uplift of the Variscan upper crust: consequences for gold deposition. Chemical Geology 194, 119–141.

Boiron, M.-C., Cathelineau, M., Dubessy, J., Bastoul, A.M., 1990. Fluids in Hercynian Au-veins from the French Variscan belt. Mineralogical Magazine 54, 231–243.

Boiron M.C., Cathelineau M., Trescases J.J., 1989. Conditions of gold-bearing arsenopyrite crystallization in the Villeranges basin, Marche-Combrailles shear zone, France. A mineralogical and fluid inclusion study. Economic Geology 84, 1340–1362.

Boiron, M.-C., Essarraj, S., Sellier, E., Cathelineau, M., Lespinasse, M., Poty, B., 1992. Identification of fluid inclusions in relation to their host microstructural domains in quartz by cathodoluminescence. Geochimica et Cosmochimica Acta 56, 175–185.

Bouchot, V., Gros, Y., Bonnemaison, M., 1989. Structural control on the auriferous shear zones of the St-Yrieix District, Massif Central, France: Evidence from the Le Bourneix and Lauricras gold deposits. Economic Geology 84, 1315–1327.

Bouchot, V., Milési, J.-P., Lescuyer, J.-L., Ledru, P., 1997. Les minéralisations aurifères de la France dans leur cadre géologique autour de 300 Ma. Chronique de la Recherche Minière 528, 13–62.

Braux, C., Moravek, P., Janatka, J., Bonnemaison, M., 1991. Comparaison entre les gîtes aurifères du socle Varisque français et du massif de Bohème. Chronique de la Recherche Minière 504, 21–39.

Burg, J.P., Van Den Driessche, J., Brun, J.P., 1994. Syn- to post-thickening extension: mode and consequences. Comptes Rendus de l'Académie des Sciences, Paris 319, 1019–1032.

Calli, M., 1988. La mine d'or de Cros Gallet – Le Bourneix (Limousin, France): géologie, structure, minéralogie et géochimie des concentrations aurifères à As, Pb, (Ag, Sb, Cu). Unpublished PhD thesis, Université Paul Sabatier, Toulouse, France.

Carignan, J., Hild, P., Mevelle, G., Morel, J., Yeghicheyan, D., 2001. Routine analyses of trace elements in geological samples using flow injection and low pressure on-line liquid chromatography coupled to ICP-MS: A study of geochemical reference materials BR, DR-N, UB-N, AN-G and GH. Geostandard Newsletters 25, 187–198.

Caron, C., 1994. Les minéralisations Pb-Zn associées au Paléozoïque inférieur d'Europe méridionale. Traçage isotopique Pb-Pb des gîtes de l'Iglesiente (SW Sardaigne) et des

Cévennes et évolution du socle encaissant par la géochronologie U-Pb, ^{40}Ar-^{39}Ar et K-Ar. Unpublished PhD thesis, Université de Montpellier II, France, 226 pp.

Cassard, D., Chabod, J.C., Marcoux, E., Bourgine, B., Castaing, C., Gros, Y., Kosakevitch, A., Moisy, M., Viallefon, L., 1994. Mise en place et origine des minéralisations du gisement filonien à Zn, Ge, Ag, (Pb, Cd) de Noailhac — Saint-Salvy (Tarn, France). Chronique de la Recherche Minière 514, 3–37.

Cathelineau, M., Boiron, M.C., Essarraj, S., Dubessy, J., Lespinasse, M., Poty, B., 1993. Fluid pressure variations in relation to multistage deformation and uplift: a fluid inclusion study of Au–quartz veins. European Journal of Mineralogy 5, 107–121.

Cathelineau, M., Boiron, M.C., Holliger, P., Poty, B., 1990. Metallogenesis of the French part of the Variscan orogen. Part II: time-space relationships between U, Au, Sn-W ore deposition and geodynamic events: mineralogical and U-Pb data. Tectonophysics 177, 59–79.

Cauuet, B., 1999, L'exploitation de l'or en Gaule à l'âge du fer. L'or dans l'antiquité de la Mine à l'Objet, Aquitania 9, 31–88.

Chalier, M., 1993. Contexte géologique, géochimique et structural des lentilles aurifères de Lauriéras et Puits Roux (Limousin central, District de Saint-Yrieix). Implications métallogéniques. Unpublished PhD thesis, University of Limoges, France.

Chalier, M., Virlogeux, D., Duthou, J.-L., 1994. Les lamprophyres du district aurifère de Saint-Yrieix (Limousin, Massif Central français). Age Rb/Sr Autunien et relations chronologiques avec le dépôt de l'or. Comptes Rendus de l'Académie des Sciences de Paris 319 (II), 1511–1518.

Chèvremont, P., Constans, J., Ledru, P., Ménillet, F., 1992. 1/50 000th Geological Map of Oradour sur Glane. BRGM, France.

Cuney, M., Friedrich, M., Blumenfeld, P., Bourguignon, A., Boiron, M.C., Vigneresse, J.L., Poty, B., 1990. Metallogenesis in the French part of the Variscan orogen. Part I: U preconcentrations in pre-Variscan and Variscan formations — a comparison with Sn, W and Au. Tectonophysics 177, 39–57.

Cuney, M., Alexandrov, P., Le Carlier de Veslud, C., Cheilletz, A., Raimbault, L., Ruffet, G., Scaillet, S., 2002. The timing of W–Sn-rare metals mineral deposit formation in the western Variscan Chain in their orogenic setting; the case of the Limousin area (Massif Central, France). In: Blundell, D., Neubauer, F., von Quadt, A. (Eds.), The Timing and Location of Major Ore Deposits in an Evolving Orogen Geological Society Special Publication, 204, pp. 213–228.

De Argollo, R., Schilling, J., 1978. Ge–Si and Ga–Al fractionation in Hawaiian volcanic rocks. Geochim. Cosmochim. Acta 42, 623–630.

Dubuisson, G., Hirn, A., Girardeau, J., Mercier, J.C.C., Veinante, J.L., 1988. Multiple Variscan nappes in Limousin, Western Massif Central, France – geophysical constraints to the geological model and geodynamic implications. Tectonophysics 147, 19–31.

Dubuisson, G., Mercier, J.C.C., Girardeau, J., Frison, J.Y., 1989. Evidence for a lost ocean in Variscan terranes of the Western Massif Central, France. Nature 337, 729–732.

Ebougué, Z., 1995. Magmas ultimes peralumineux à métaux rares (Be, Li, Nb, Ta, Sn) : mise en évidence de processus de différenciation extrême dans des dykes (Région de Blond, Massif Central français). Unpublished PhD thesis, University Henri Poincaré Nancy 1, France.

El Jarray A., 1993. Circulations fluides et alterations hydrothermales associées aux minéralisations à U (As, F) dans le massif de Saint Sylvestre (NW du massif Central français). Unpublished PhD thesis, INPL, Nancy, France, 324 p.

El Jarray, A., Boiron, M.C., Cathelineau, M., 1994. Percolation microfissurale de vapeurs aqueuses dans le granite de Peny (Massif de Saint Sylvestre, Massif Central) : relation avec la dissolution du quartz. Comptes-Rendus de l'Académie des Sciences, Paris, 318, 1095-1102.

El Korh, A., Deloule, E., Luais, B., Boiron, M.C., Bastian, L., Vigier, N. (in press). Lithium behaviour and isotope fractionation during fluid-rock interactions in Variscan oceanic suture zones: Limousin ophiolite and Ile de Groix high-pressure terrane (France). Journal of Petrology, doi: 10.1093/petrology/egz060

El Korh, A., Luais, B., Boiron, M.C., Deloule, E., Cividini, D., 2017. Investigation of Ge and Ga exchange behaviour and Ge isotopic fractionation during subduction zone metamorphism. Chemical Geology 449, 165–181.

Essarraj, S., Boiron M.C., Cathelineau, M., Fourcade, S., 2001. Multistage deformation of Au-quartz veins: Evidence for late gold introduction from microstructural, isotopic and fluid inclusion studies. Tectonophysics, 336, 79–99.

Faure, M., 1995. Late orogenic Carboniferous extensions in the Variscan French Massif Central. Tectonics 14 (1), 132–153.

Faure, M., Pons, J., 1991. Crustal thinning recorded by the shape of Namurian–Westphalian leucogranite in the Variscan belt of the northern Massif Central, France. Geology 19, 730–733.

Faure, M., Lardeaux, J.M., Ledru, P., 2009. A review of the pre-Permian geology of the Variscan French Massif Central. Comptes Rendus Geosciences 341, 202–213.

Faure, M., Li, X. H., Lin, W., 2017. The northwest-directed “Bretonian phase” in the French Variscan Belt (Massif Central and Massif Armoricain): A consequence of the Early Carboniferous Gondwana–Laurussia collision. Comptes Rendus Géoscience, 349, 126–136.Floc'h, J.P., Santallier, D., Henry, B., 1984. La série limousine: réflexion axée sur une synthèse géologique régionale et son utilisation pour la prospection de l'or. Chronique de la Recherche Minière 474, 5–10.

Franke, W., 1992. Phanerozoic structures and events in Central Europe. In: Blundell, D., Freeman, R., Mueller, S. (Eds). A continent revealed. The European geotraverse. Cambridge University Press, Cambridge, UK, 164–180.

Franke, W., Cocks, L.R.M., Torsvik, T.H., 2017. The Palaeozoic Variscan oceans revisited. Gondwana Research 48, 257–284.

Gibert, F., Moine, B., Béziat, P., 1988. Les gneiss à silicates calciques minéralisés en W-Sn dans la série des schistes X, à la terminaison orientale de la Montagne Noire. Résultats préliminaires. In: Johan, Z., Ohnenstetter, D. (Eds), Gisements métallifères dans leur contexte géologique. Doc BRGM 158 (1): 219–244.

Gibert, F., Moine, B., Schott, J., Dandurand, J.-L., 1992. Modeling of the transport and deposition of tungsten in the scheelite-bearing calc-silicate gneisses of the Montagne Noire, France. Contributions to Mineralogy and Petrology 112, 371–384.

Girardeau, J., Dubuisson, G., Mercier, J.-C.C., 1986. Cinématique de mise en place des ophiolites et nappes crystallophiliennes du Limousin, Ouest du Massif Central francais. Bulletin de la Société Géologique de France 2, 849–860.

Harlaux, M., Romer, R.L., Mercadier, J., Morlot, C., Marignac, C., Cuney, M., 2018. 40 Ma of hydrothermal W mineralization during the Variscan orogenic evolution of the French Massif Central revealed by U-Pb dating of wolframite. Mineralium Deposita 53, 21–51.

Holliger, P., Cuney, M., Friedrich, M., Turpin, L., 1986. Ages carbonifères de l'unité de Brâme du complexe granitique peralumineux de Saint-Sylvestre (NO Massif Central) défini par les données isotopiques sur zircon et monazite. Comptes Rendus de l'Académie des Sciences, Paris 303, 1309–1314.

Jenner, F.E., O'Neill, H.S.C., 2012. Analysis of 60 elements in 616 ocean floor basaltic glasses. Geochemistry Geophysics Geosystems 13, Q02005, doi: 10.1029/ 2011GC004009.

Kretz, R., 1983. Symbols for rock-forming minerals. American Mineralogist 68, 277–279.

Kroner, U., Romer, R.L., 2013. Two plates – many subduction zones: the Variscan orogeny reconsidered. Gondwana Research 24, 298–329.

Lardeaux, J.M., Schulmann, K., Faure, M., Janoušek, V., Lexa, O., Skrzypek, E., Edel, J.B., Štípská, P., 2014. The Moldanubian zone in the French Massif Central, Vosges/Schwarzwald and Bohemian Massif revisited: differences and similarities. Geological Society, London, Special Publications 405, 7–44.

Leblanc, M., 1989. L'or du domaine Varisque: un héritage Cambro-Ordovicien? Comptes-Rendus de l'Académie des Sciences, Paris 309, 569–573.

Le Carlier de Veslud, C., Alexandre, P., Ruffet, G., Cuney, M., Cheilletz, A., 2013. A two-stage exhumation in Western French Massif Central: new geochronological evidences of syn-collisional extension. Lithos 175-176, 1–15.

Le Carlier de Veslud, C., Cuney, M., Royer, J.J., Floc'h, J.P., Améglio, L., Alexandrov, P., Vigneresse, J.L., Chèvremont, P., Itard, Y., 2000. Relationships between granitoids and mineral deposits: 3-D modelling of the Variscan Limousin province (NW French Massif Central). Transactions of the Royal Society of Edinburgh: Earth Sciences 91, 283–301.

Ledru, P., Lardeaux, J.M., Santallier, D., Autran, A., Quenardel, J.M., Floc'h, J.P., Lerouge, G., Maillet, N., Marchand, J., Ploquin, A., 1989. Où sont les nappes dans le Massif Central Français? Bulletin de la Société Géologique de France 3, 605–618.

Ledru, P., Autran, A., Santallier, D., 1994. Lithostratigraphy of Variscan terranes in the French Massif Central: a basis for paleogeographical reconstructions. In: Keppie, J.D. (Ed). Pre-mesozoic geology in France and related areas. Springer-Verlag, Berlin Heidelberg, 276–288.

Luais, B., Le Carlier de Veslud, C., Géraud, Y., Gauthier-Lafaye, F., 2009. Comparative behavior of Sr, Nd and Hf isotopic systems during fluid-related deformation at middle crust levels. Geochimica et Cosmochimica Acta 73, 2961–2977.

Marcoux, E., Bonnemaison, M., 1988. La géochimie isotopique du plomb et la prospection de l'or en France. In: Johan, Z., Ohnenstetter, D. (Eds), Gisements métallifères dans leur contexte géologique. Documents du Bureau de Recherches Géologiques et Minières 158, 489–508.

Marignac, C., Cuney, M., 1999. Ore deposits of the French Massif Central: insight into the metallogenesis of the Variscan collision belt. Mineralium Deposita 34, 472–504.

McDonough, W.F., Sun, S.S., 1995. The composition of the earth. Chemical Geology 120, 223–253.

Merlet, C., 1994. An accurate computer correction program for quantitative electron probe microanalysis. Mikrochimica Acta 114/115, 363–376.

Nance, R.D., Gutiérrez-Alonso, G., Keppie, J.D., Linnemann, U., Murphy, J.B., Quesada, C., Strachan, R.A., Woodcock, N.H., 2010. Evolution of the Rheic Ocean. Gondwana Research 17, 194–222.

Pastier, P., 1992. Typologie des granitoïdes de l'Ouest du Massif Central Français. Géochimie et minéralogie des granites alumineux. Evolution épigénétique dans le district de Saint-Yrieix. Unpublished PhD thesis, University of Limoges, France.

Pin, C., Vielzeuf, D., 1983. Granulites and related rocks in Variscan median Europe: a dualistic interpretation. Tectonophysics 93, 47–74.

Raimbault, L., 1999. Tin–tungsten vein mineralisation at Moulin-Barret, France. In: Stanley, et al. (Ed.), Mineral Deposits: Processes to Processing. Balkema, Rotterdam, pp. 417–420.

Romer, R.L., Kroner, U., 2015. Sediment and weathering control on the distribution of Paleozoic magmatic tin-tungsten mineralization. Mineralium Deposita 50, 327–338.

Romer, R.L., Kroner, U., 2016. Phanerozoic tin and tungsten mineralization – Tectonic controls on the distribution of enriched protoliths and heat sources for crustal melting. Gondwana Research 31, 60–95.

Rouxel, O., Dobbek, N., Ludden, J., Fouquet, Y., 2003. Iron isotope fractionation during oceanic crust alteration. Chemical Geology 202, 155–182.

Rouxel O.J., Luais B., 2017. Germanium Isotope Geochemistry. Reviews in Mineralogy & Geochemistry 82, 601–656.

Santallier, D. 1981. Les roches basiques de la série métamorphique du Bas-Limousin, Massif Central (France). Thèse d'État, Université d'Orléans (France).

Santallier, D., Briand, B., Ménot, R.P., Piboule, M., 1988. Les complexes leptyno-amphiboliques (C.L.A.): revue critique et suggestions pour un meilleur emploi de ce terme. Bulletin de la Société Géologique de France 8 (IV), 3–12.

Scaillet, S., Cheilletz, A., Cuney, M., Farrar, E., Archibald, A.D., 1996a. Cooling pattern andmineralisation history of the Saint Sylvestre and Western Marche leucogranite pluton, French Massif Central: I. $^{40}Ar/^{39}Ar$ isotopic constraints. Geochimica et Cosmochimica Acta 60 (23), 4653–4671.

Scaillet, S., Cuney, M., Le Carlier de Veslud, C., Cheilletz, A., Royer, J.J., 1996b. Cooling pattern and mineralisation history of the Saint Sylvestre and Western Marche leucogranite pluton, French Massif Central: II. Thermal modelling and implications for the mechanisms of U-mineralization. Geochimica et Cosmochimica Acta 60 (23), 4673–4688.

Soufi, M., 1988. Etude des magmatismes leucogranitique et ongonitique de Blond (Haut Limousin, Massif Central Français). Relations avec une mise en place syntectonique du massif granitique. Unpublished PhD thesis, University of Nancy, France, 304p.

Spandler, C.J., Hermann, J., Arculus, R.J., Mavrogenes, J.A., 2004. Geochemical heterogeneity and element mobility in deeply subducted oceanic crust; insights from high-pressure basic rocks from New Caledonia. Chemical Geology 206, 21–42.

Stampfli, G.M., von Raumer, J.F., Borel, G., 2002. The Paleozoic evolution of pre-Variscan terranes: From Gondwana to the Variscan collision. In: Martínez Catalán, J.R., Hatcher, R.D. Jr, Arenas, R., Díaz Garcia, F. (eds). Variscan-appalachian dynamics: the building of the late paleozoic basement. Geological Society of America Special Papers 364, 263–280.

Stampfli, G.M., von Raumer, J.F., Wilhem, C., 2011. The distribution of Gondwana derived terranes in the early Paleozoic. In: Gutiérrez Marco, J.C., Rábano, I., García-Bellido, I. (Eds.) The ordovician of the world. Instituto Geológico y Minero de España, Madrid, Cuadernos del Museo Geominero 14, 567–574.

Stephan, T., Kroner, U., Romer, R. L., Rösel, D., 2019. From a bipartite Gondwana shelf to an arcuate Variscan belt: The early Paleozoic evolution of northern Peri-Gondwana. Earth-science reviews 192, 491–512.

Stussi, J.M., La Roche, H., 1984. Le magmatisme granitique orogénique de la chaîne varisque française. Typologie chimique et répartition spatiale. Comptes Rendus de l'Académie des Sciences, Paris 298, 43–48.

Sun, S.S., McDonough, W.F., 1989. Chemical and isotopic systematics of oceanic basalts: implications for mantle composition and processes. In: Saunders, A.D., Norry, M.J. (Eds.), Magmatism in ocean basins: Geological Society Special Publication, 42, pp. 313–345.

Taylor, S.R., McLennan, S.M., 1981. The composition and evolution of the continental crust: rare earth element evidence from sedimentary rocks. Philosophical Transactions of the Royal Society of London A301, 381–399.

Vallance, J., Boiron, M.-C., Cathelineau, M., Fourcade, S., Varlet, M., Marignac, C., 2004. The granite hosted gold deposit of Moulin de Chéni (Saint-Yrieix district, Massif Central, France): petrographic, structural, fluid inclusion and oxygen isotope constraints, Mineralium Deposita 39, 265–281.

Vallance, J., Cathelineau, M., Marignac, C., Boiron, M.-C., Fourcade, S., Martineau, F., Fabre, C., 2001. Microfracturing and fluid mixing in granites: W-(Sn) ore deposition at Vaulry (NW French Massif Central). Tectonophysics 336, 43–61.

von Raumer, J., Bussy, F., Schaltegger, U., Schulz, B., and Stampfli, G.M., 2013, Pre-Mesozoic Alpine basements – their place in the European Paleozoic framework. Geological Society of America Bulletin 125, 89–108.

von Raumer, J., Stampfli, G. M., Arenas, R. & Martínez, S.S., 2015. Ediacaran to Cambrian oceanic rocks of the Gondwana margin and their tectonic interpretation. International Journal of Earth Sciences 104, 1107–1121.

Wolf, M., Romer, R.L., Franz, L., López-Moro, F.J., 2018. Tin in granitic melts: The role of melting temperature and protolith composition. Lithos 310, 20–30.

LIST OF TABLES

Table 1: Description and mineral assemblage of the studied samples

Table 2: Whole rock major and trace element composition of serpentinites, amphibolites, UHP eclogite and gneiss

Table 3: Trace element abundances in the mineral assemblage of serpentinites

Table 4: Trace element abundances in the mineral assemblage of amphibolites

Table 5: Trace element abundances in the mineral assemblage of the UHP eclogite

Table 6: Trace element abundances in the mineral assemblage of granites and gneiss

Electronic appendix: Supplementary tables of detailed major and trace element analyses of minerals

LIST OF FIGURES

Figure 1. (a) General sketch of the European Western Variscan Belt (after Berger et al., 2005; Ballèvre et al., 2014; El Korh et al., in press). (b) Geological map of the French Massif Central (after Faure et al., 2009; Lardeaux et al., 2014). The black rectangle corresponds to the studied area in Fig. 2. Profiles AA' and B'B corresponds to the cross-sections represented in Fig. 10.

Figure 2. Geological map of the Limousin area. After Le Carlier de Veslud et al. (2000), Vallance et al. (2004), Berger et al. (2005, 2010) and El Korh et al. (in press).

Figure 3. Photomicrographs of representative studied samples. (a) serpentinite FLOT2a (La Flotte); (b) serpentinite CLUZ6 (Le Cluzeau); (c) serpentinite LAU1 (St-Laurent); (d) amphibolite CLUZ4 (Le Cluzeau); (e) granite IGAR744 (St-Sylvestre); (f) granite VAU6 (Vaulry). Mineral abreviations are from Kretz (1983).

Figure 4. Primitive mantle-normalised multi-element diagrams for incompatible trace elements (a) and for the metals of interest (b) in serpentinites, amphibolites, UHP eclogite L04-143, and orthogneiss GNEISS-SY-1, in comparison with N-MORB and OIB (Sun and Mc Donough, 1989), upper continental crust (Taylor and McLennan, 1981) and mean value for ocean floor basalts (Jenner and O'Neill, 2002). Data for eclogite L04-143 are from Berger et al. (2010) and this study. Normalisation data for the primitive mantle ("pyrolite") are from McDonough and Sun (1995).

Figure 5. Trace element distribution in serpentinites. Average abundances are represented by symbols. The grey bar represents the range of trace element concentrations. Empty fields correspond to data below detection limit.

Figure 6. Trace element distribution in amphibolites. Average abundances are represented by symbols. The grey bar represents the range of trace element concentrations. Empty fields correspond to data below detection limit.

Figure 7. Trace element distribution in the UHP eclogite. Average abundances are represented by symbols. The grey bar represents the range of trace element concentrations. Empty fields correspond to data below detection limit.

Figure 8. Trace element distribution in granites and gneiss. Average abundances are represented by symbols. The grey bar represents the range of trace element concentrations. Empty fields correspond to data below detection limit.

Figure 9. W vs. Sn, Ge vs. Zn, and Cr vs. V abundances in micas (biotite, muscovite) of granites and gneiss from the studied area. All data are individual LA-ICPMS measurements. Dashed lines: fields of data for muscovite; solid lines: fields of data for biotite. Data are sorted according to the three main districts: Sn–W (Vaulry), Au (Cheni, Lauriéras, St-Yrieix) and U (La Marche, St-Sylvestre). While W vs. Sn and Ge vs. Zn variations show a clear geographical correlation, the Cr vs. V variation appears to be independent from the locality.

Figure 10. Simplified S to N and SW to NE cross-sections through the FMC (profiles AA' and B'B in Figure 1) (modified after Lardeaux et al., 2014). Sn and W variations in micas are reported for the different studied granite massifs. Sn and W concentrations in serpentinites, amphibolites and UHP eclogites are generally low and were not included in the figure (see Tables 3 to 5). Age data are from Holliger et al. (1986), Bouchot et al. (1989, 1997), Cathelineau et al. (1990), Chalier (1994), Scaillet et al. (1996a, 1996b), Marignac and Cuney (1999), Alexandrov (2000), Alexandrov et al. (2002), Le Carlier de Veslud et al. (2000, 2013), Berger et al. (2010) and Harlaux et al. (2018).

Figure 1 (colour)
Click here to download high resolution image

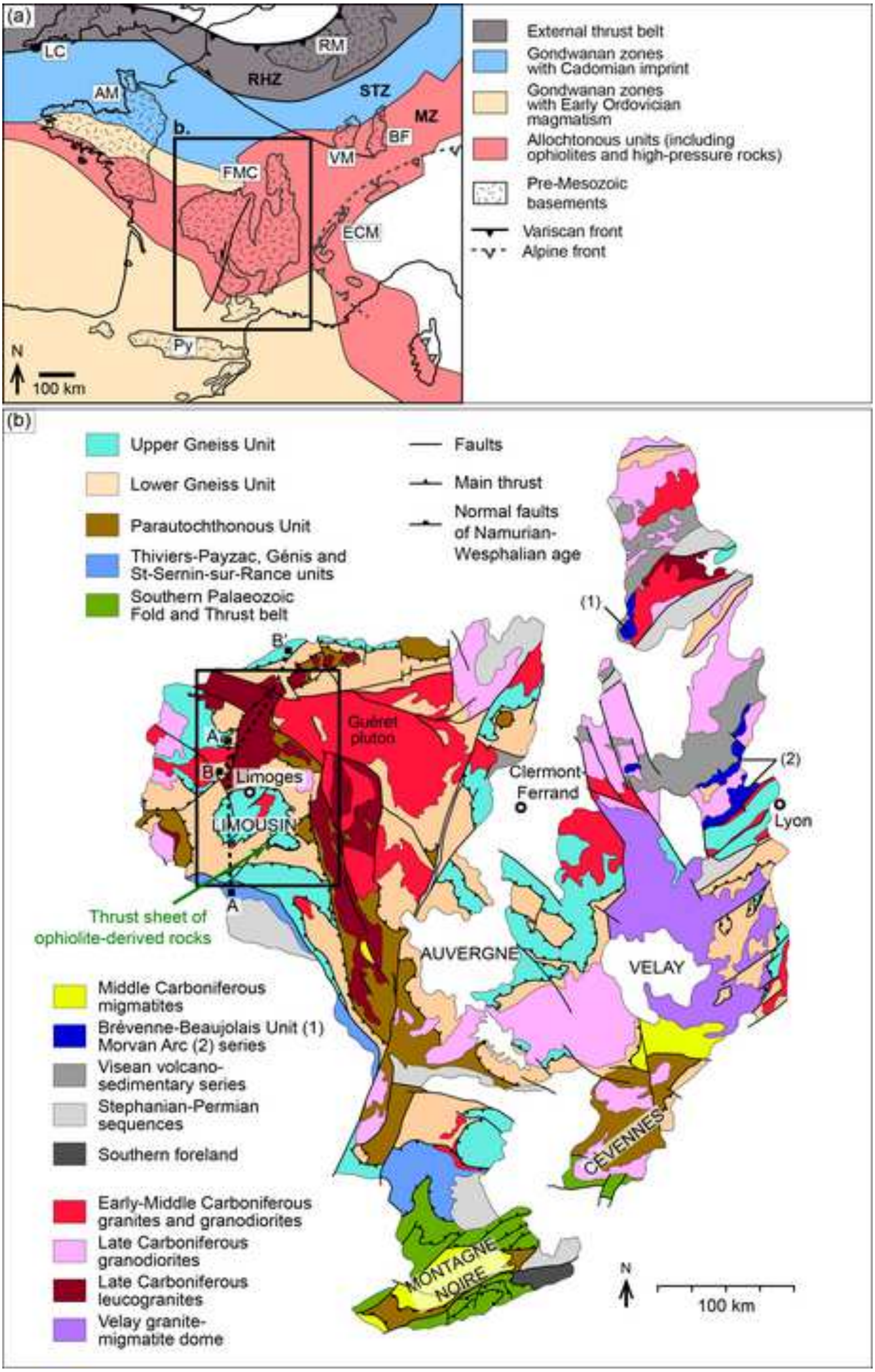

Figure 1 (greyscale)

Click here to download high resolution image

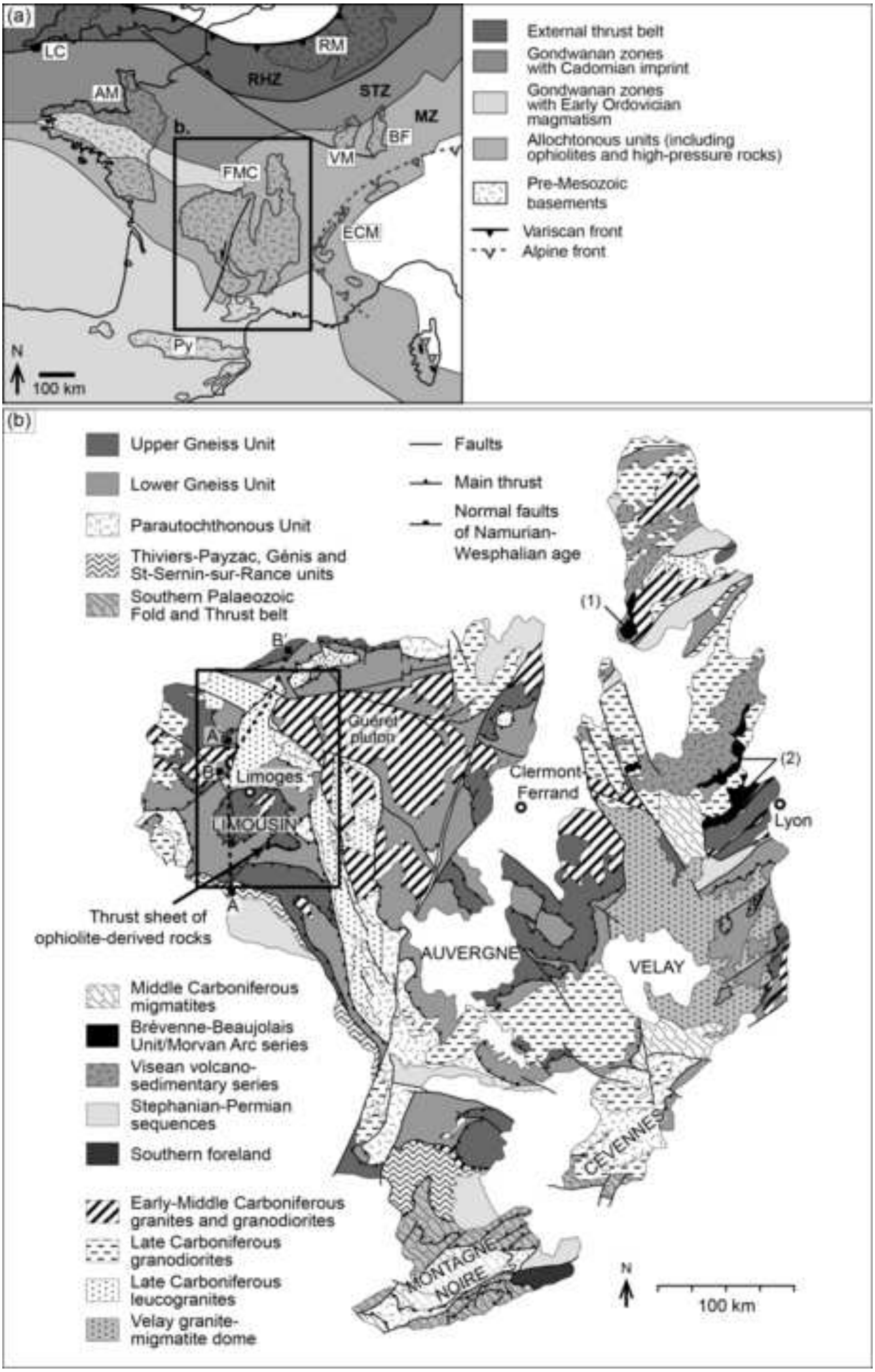

Figure 2 (colour)

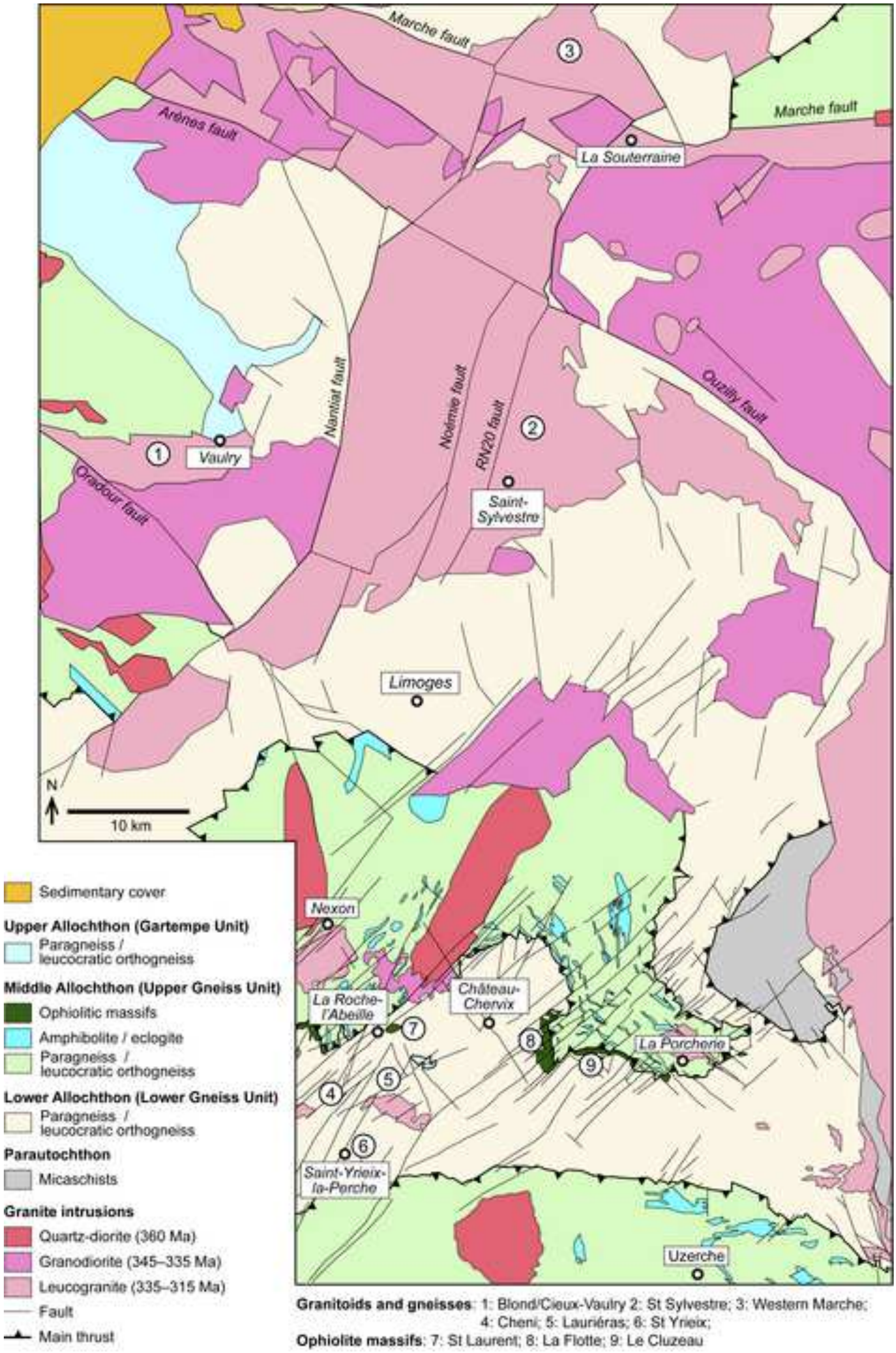

Figure 2 (greyscale)

Click here to download high resolution image

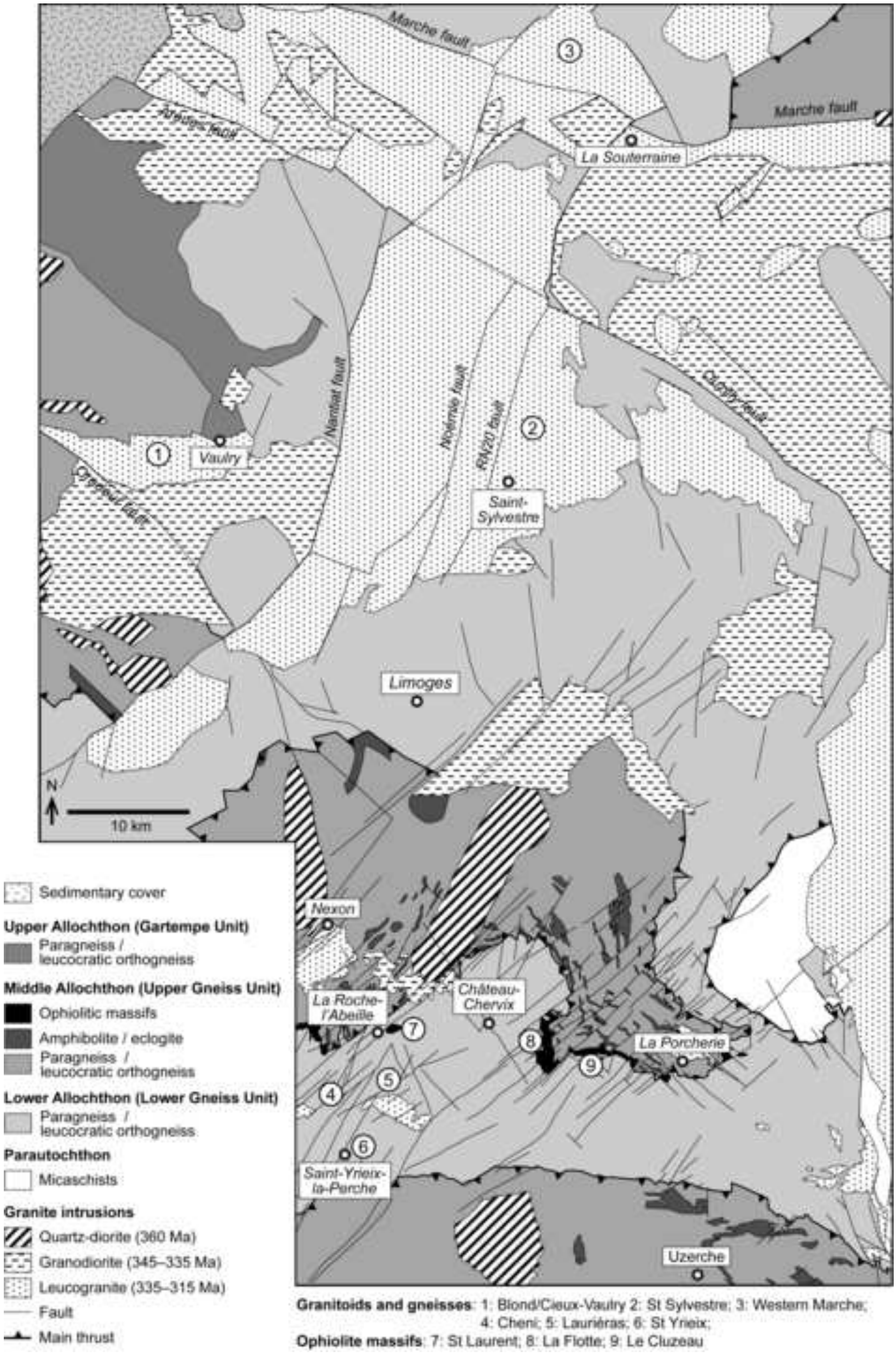

Figure 3 (colour)
[Click here to download high resolution image]

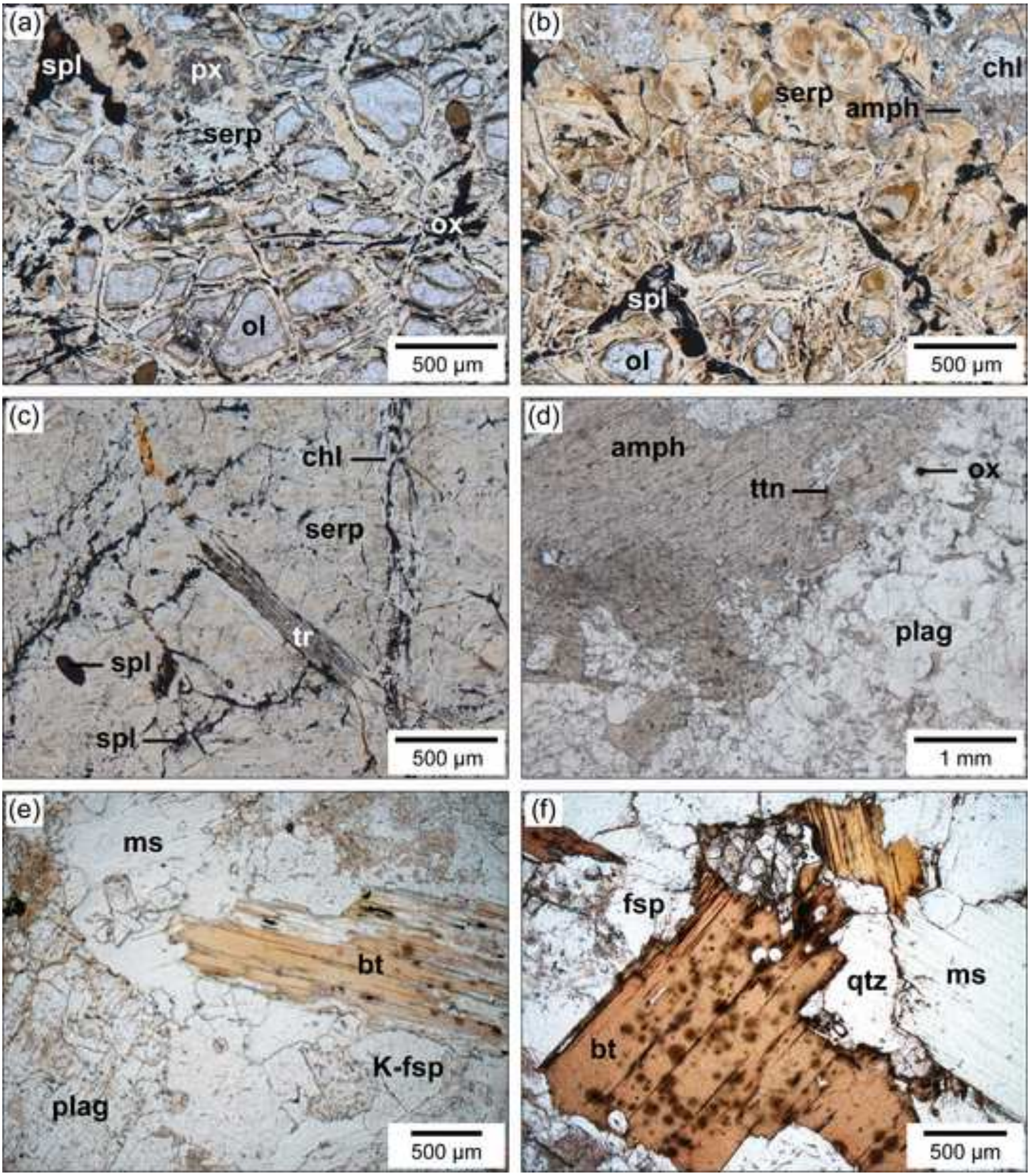

Figure 3 (greyscale)

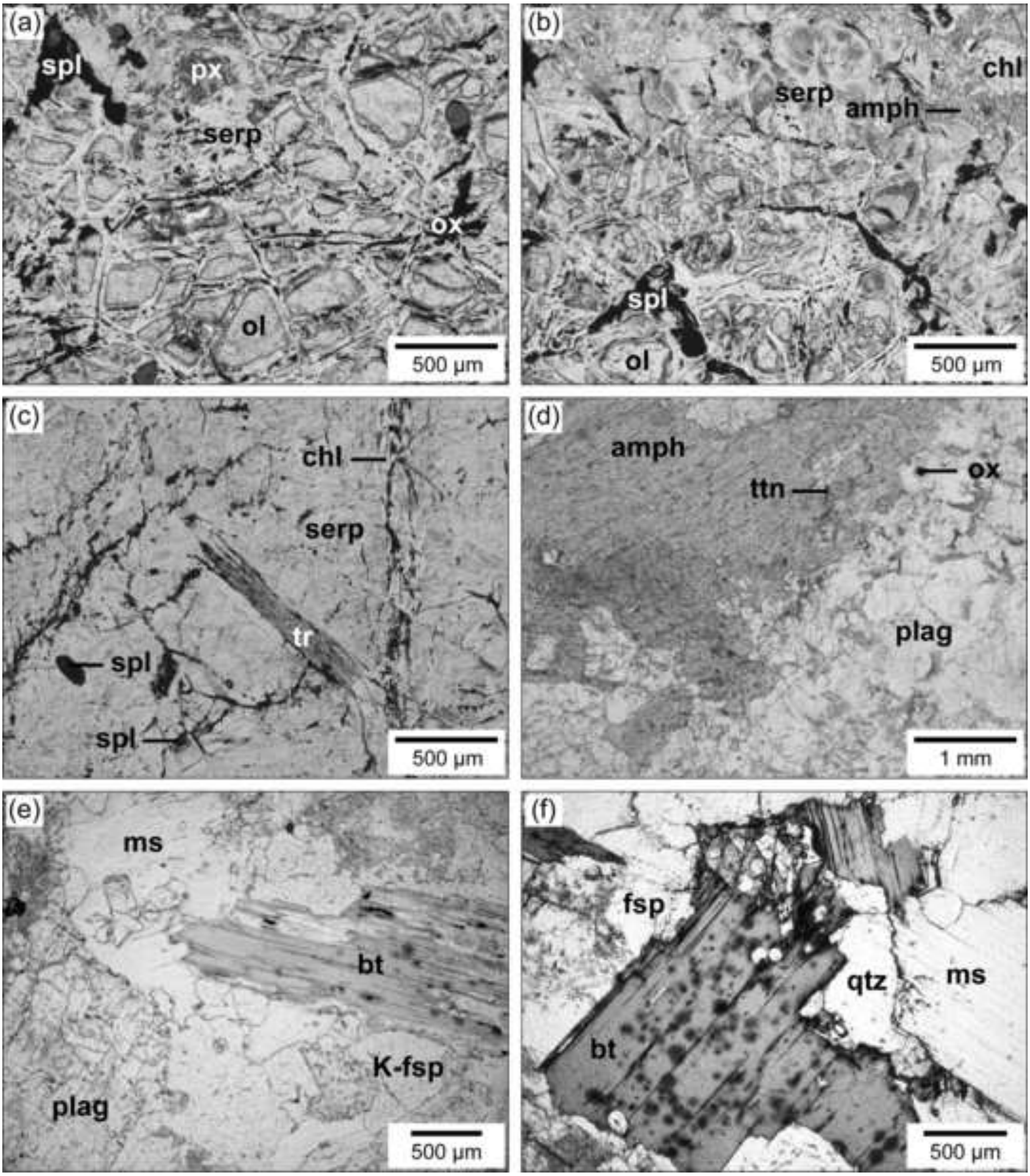

Figure 4 (colour)
Click here to download high resolution image

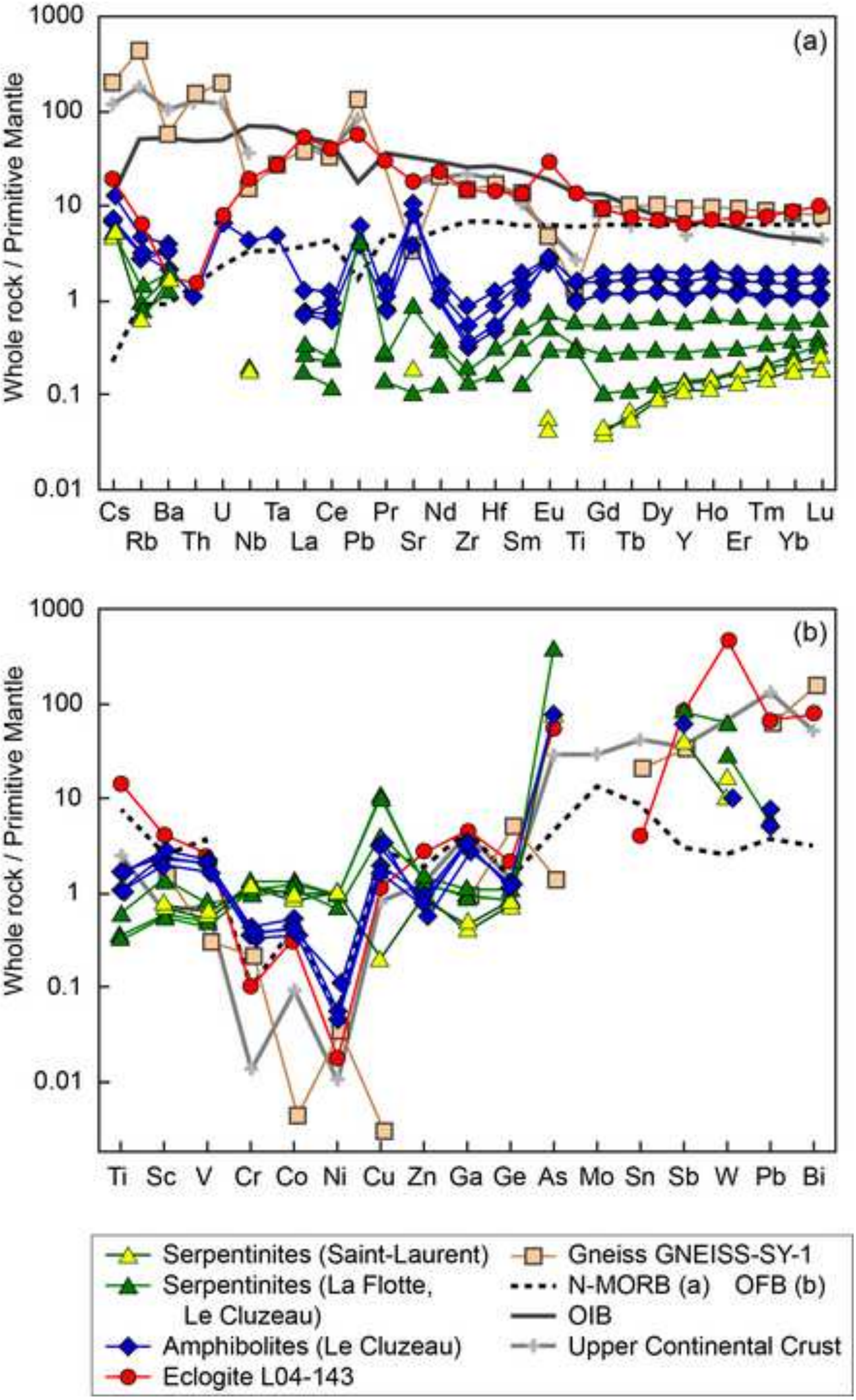

Figure 4 (greyscale)

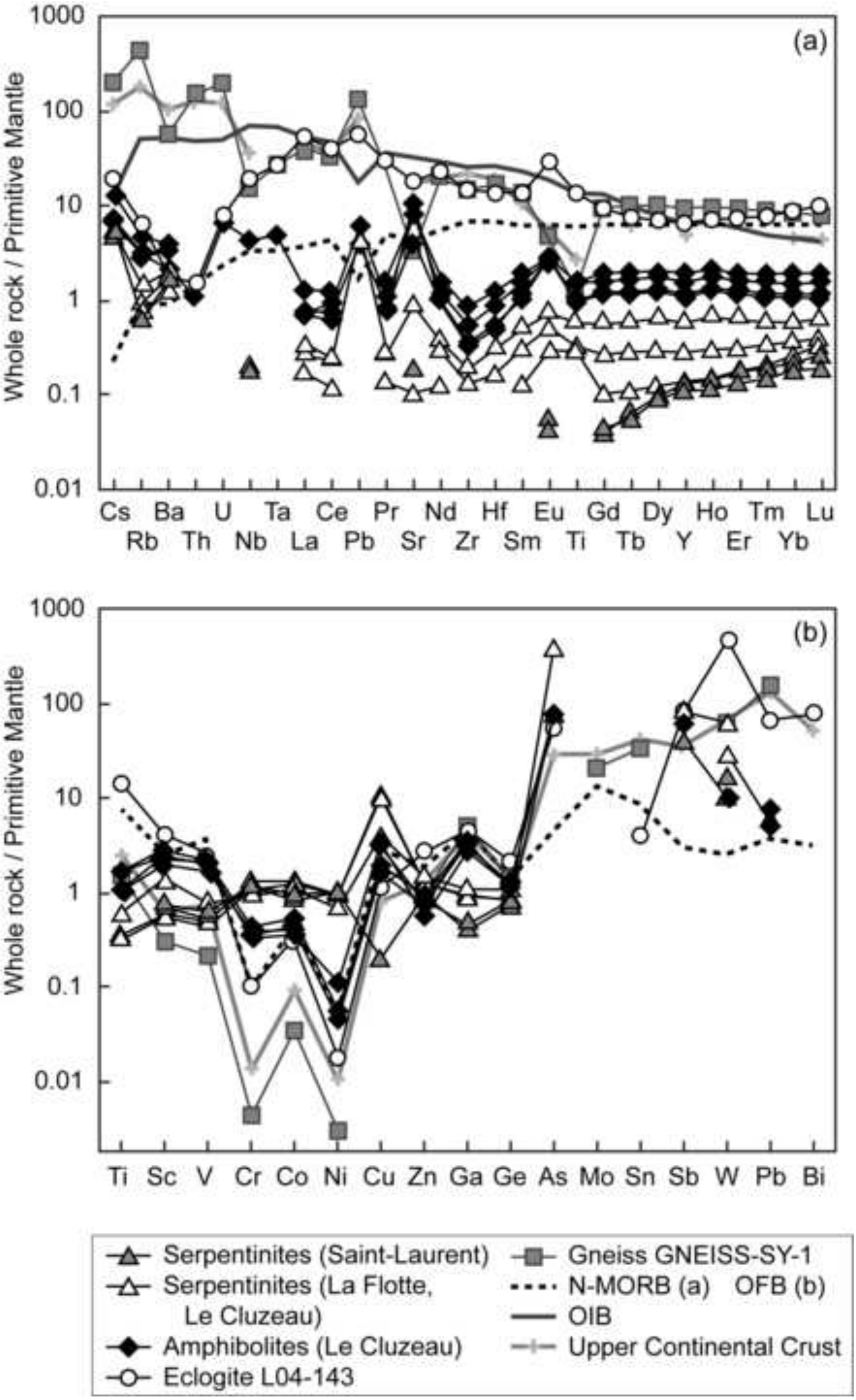

Figure 5 (colour)
Click here to download high resolution image

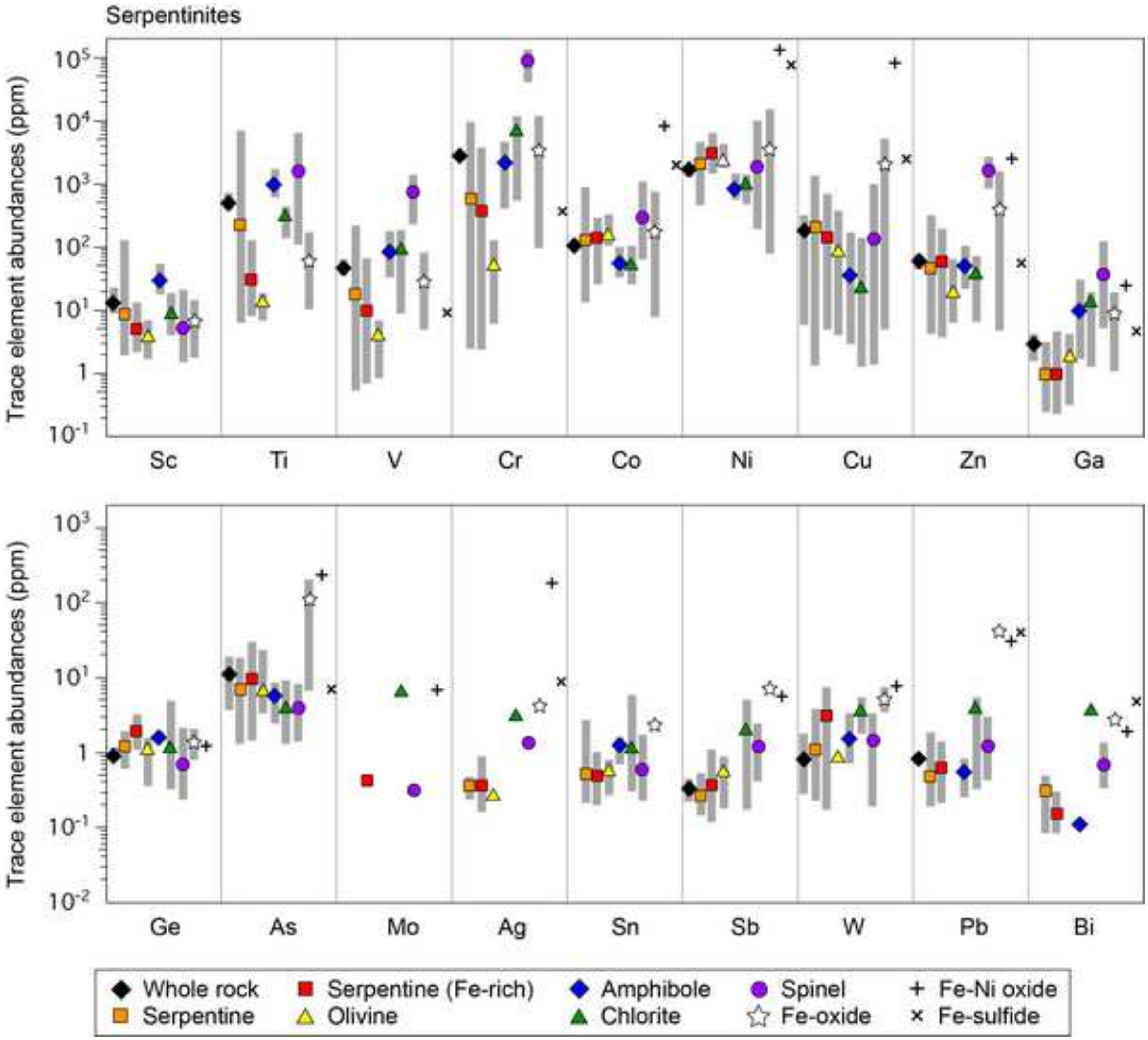

Figure 5 (greyscale)

Click here to download high resolution image

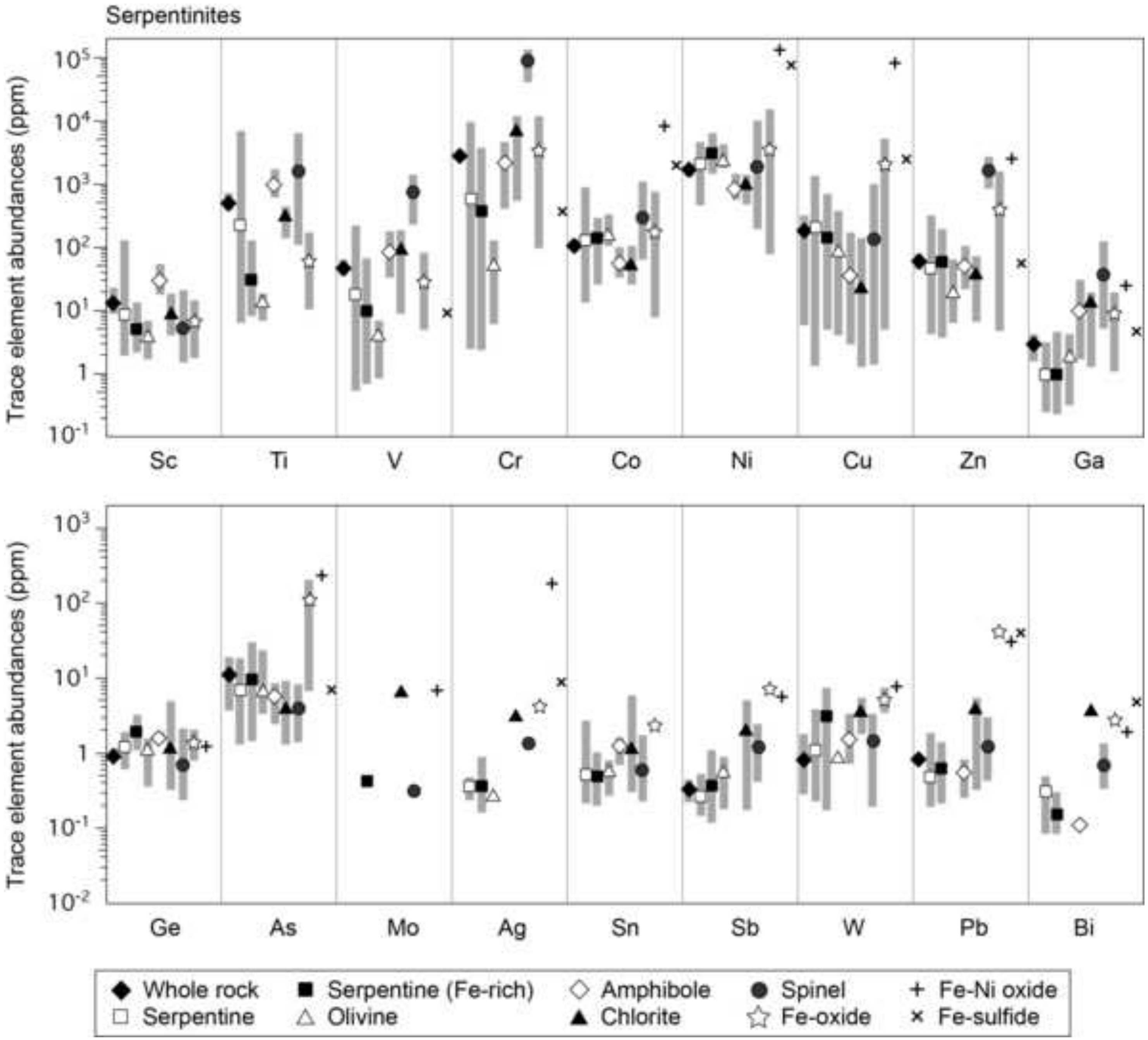

Figure 6 (colour)
Click here to download high resolution image

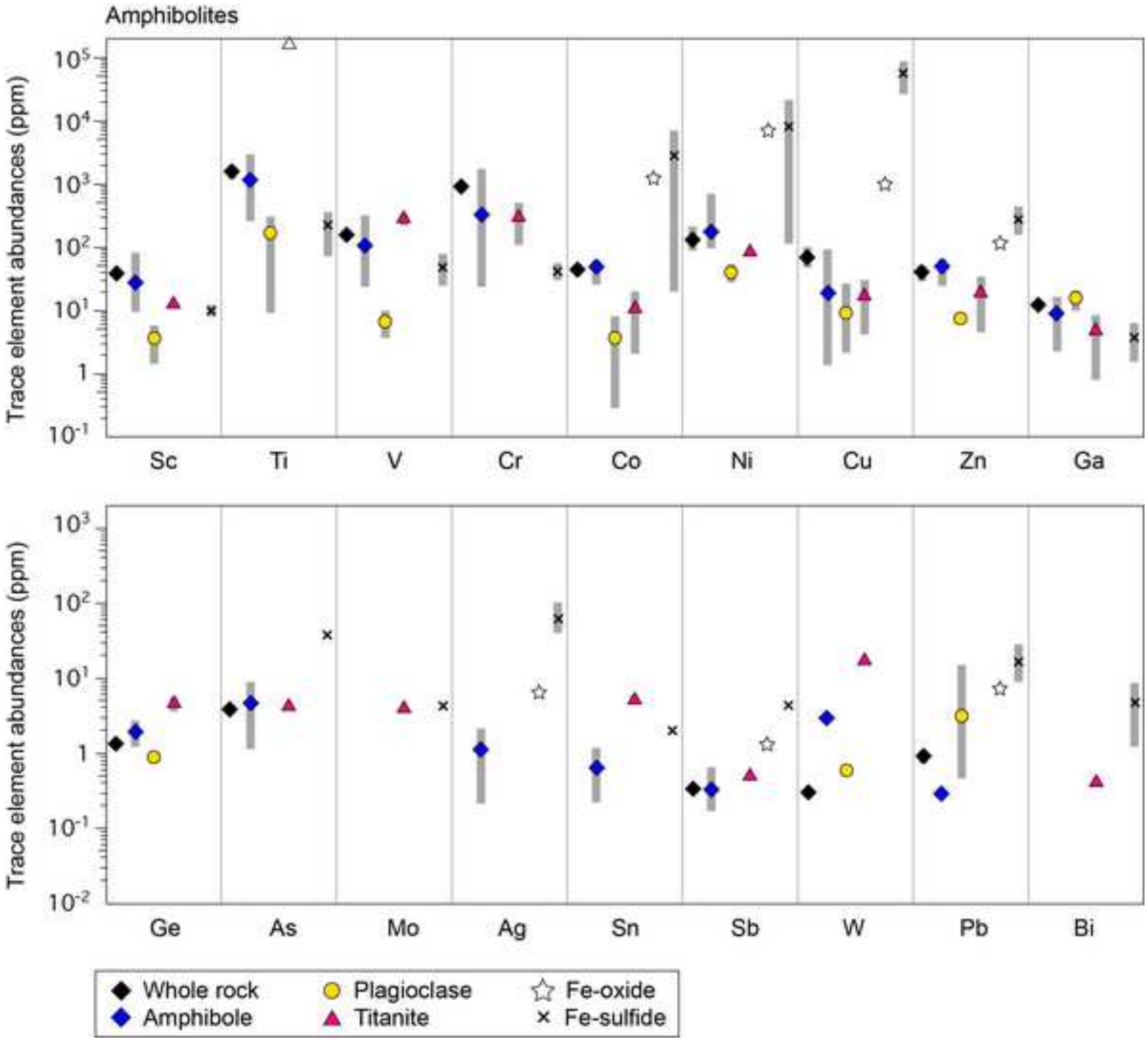

Figure 6 (greyscale)

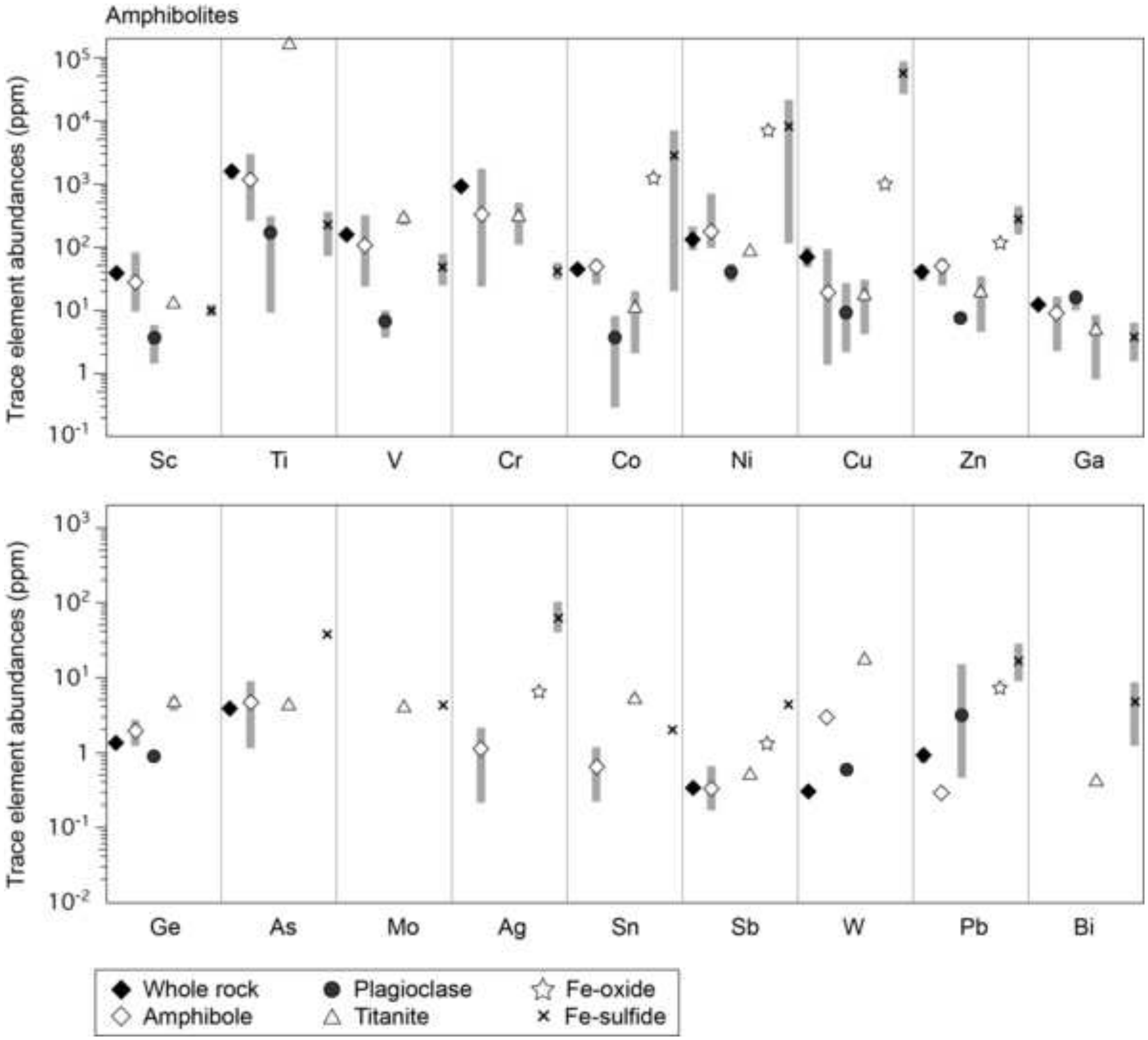

Figure 7 (colour)
Click here to download high resolution image

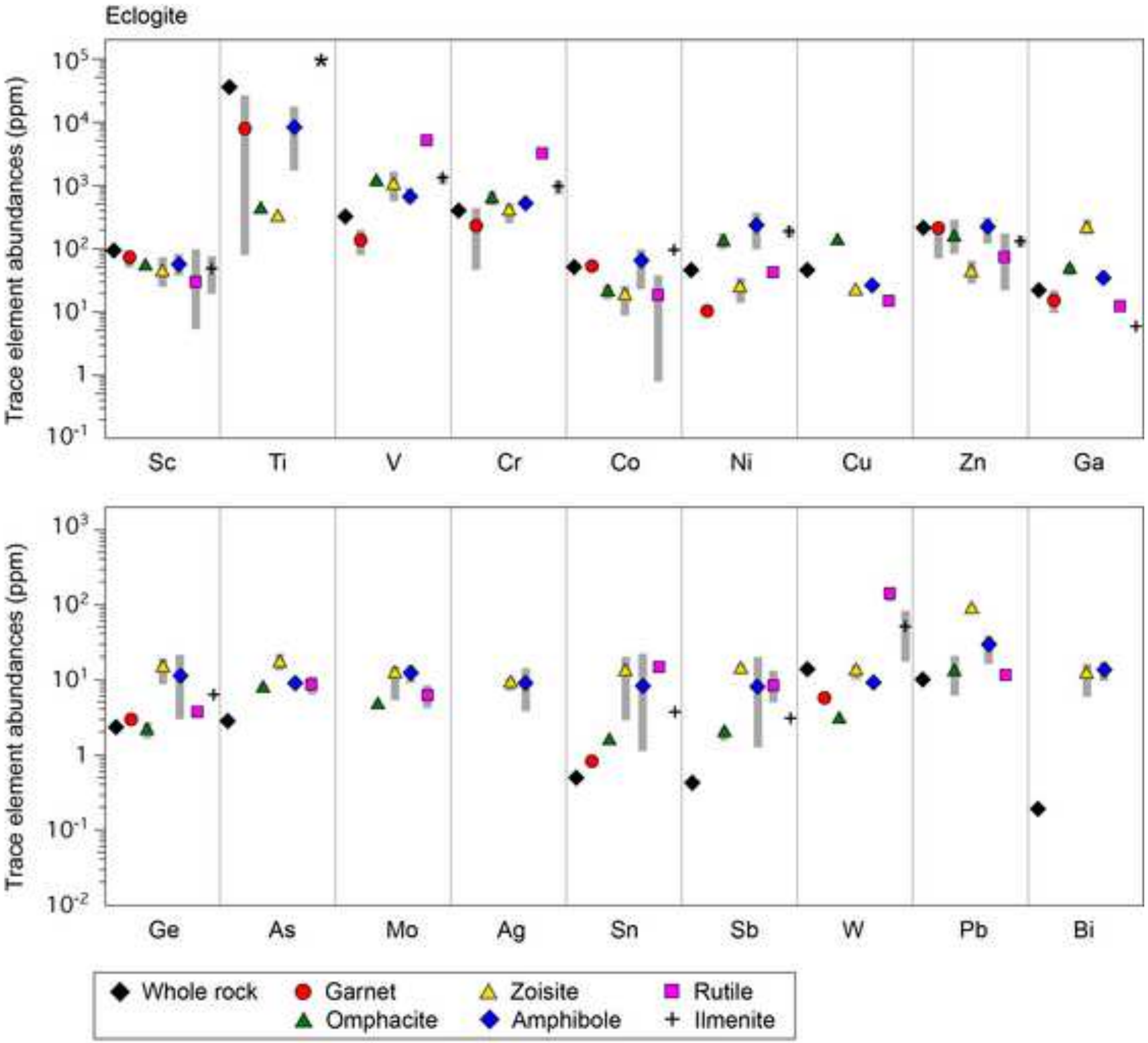

* Ti is present as major element (> 4×10^5 ppm) in rutile and ilmenite.

Figure 7 (greyscale)
Click here to download high resolution image

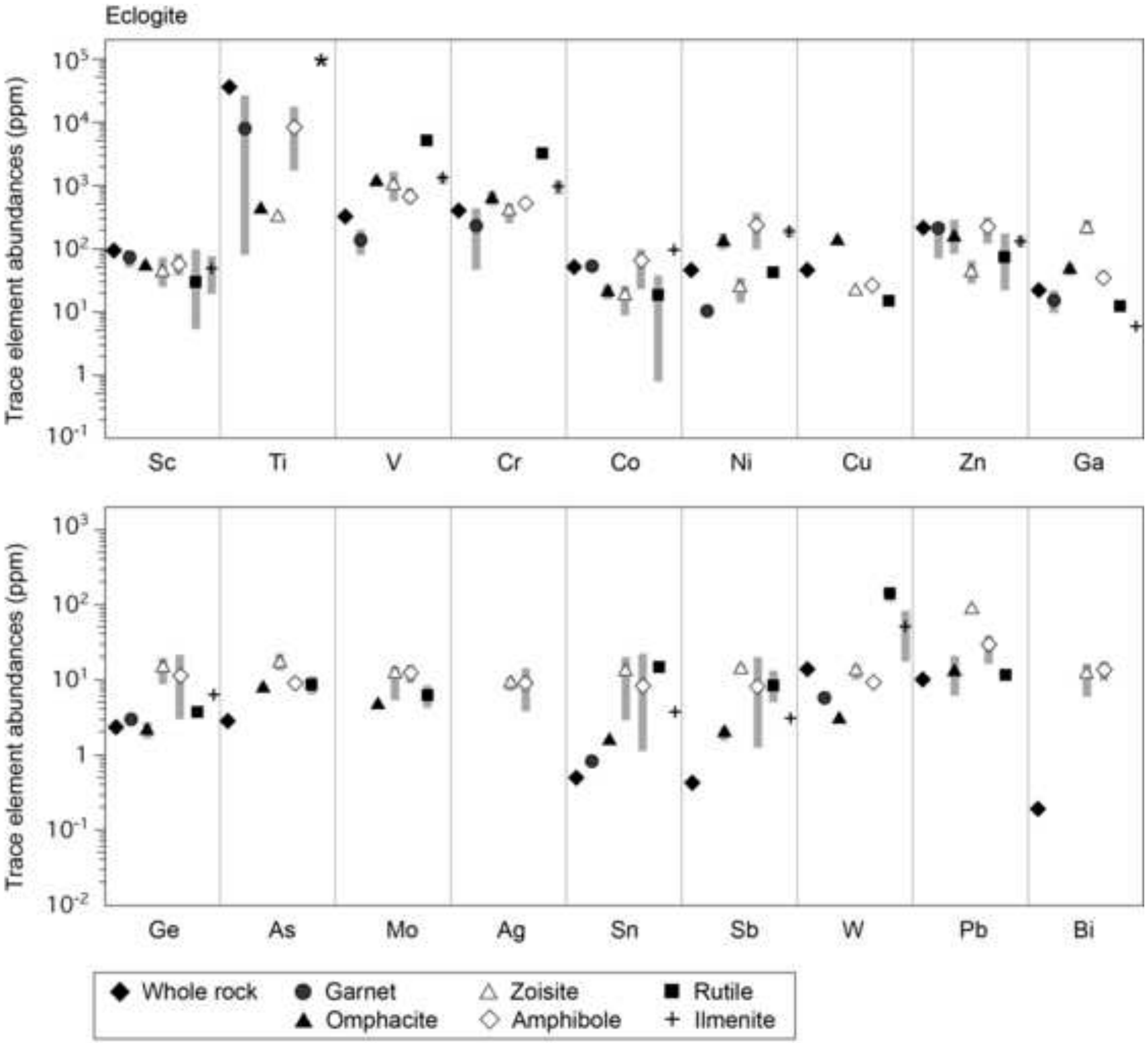

★ Ti is present as major element (> 4×10^5 ppm) in rutile and ilmenite.

Figure 8 (colour)
Click here to download high resolution image

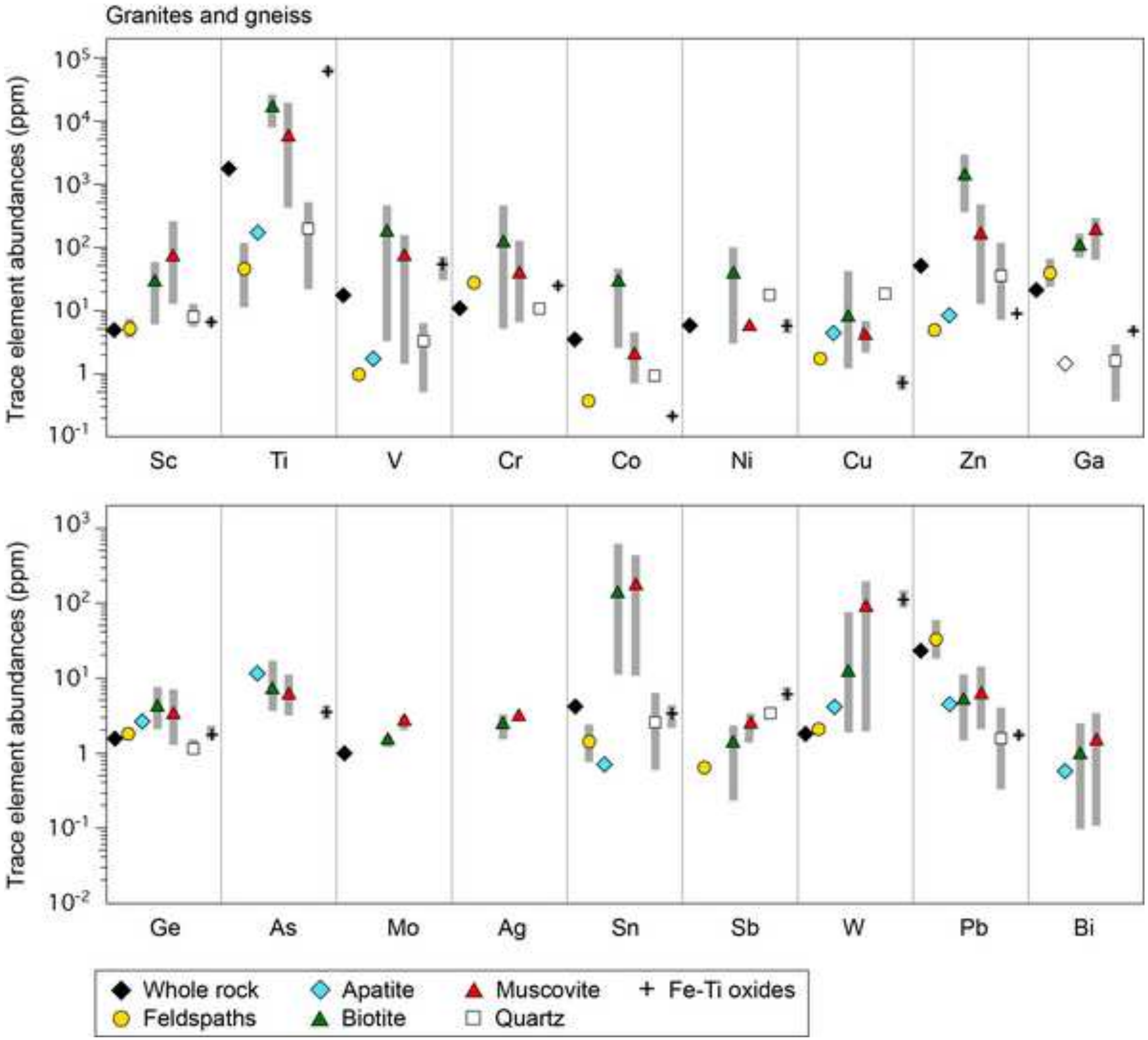

Figure 8 (greyscale)

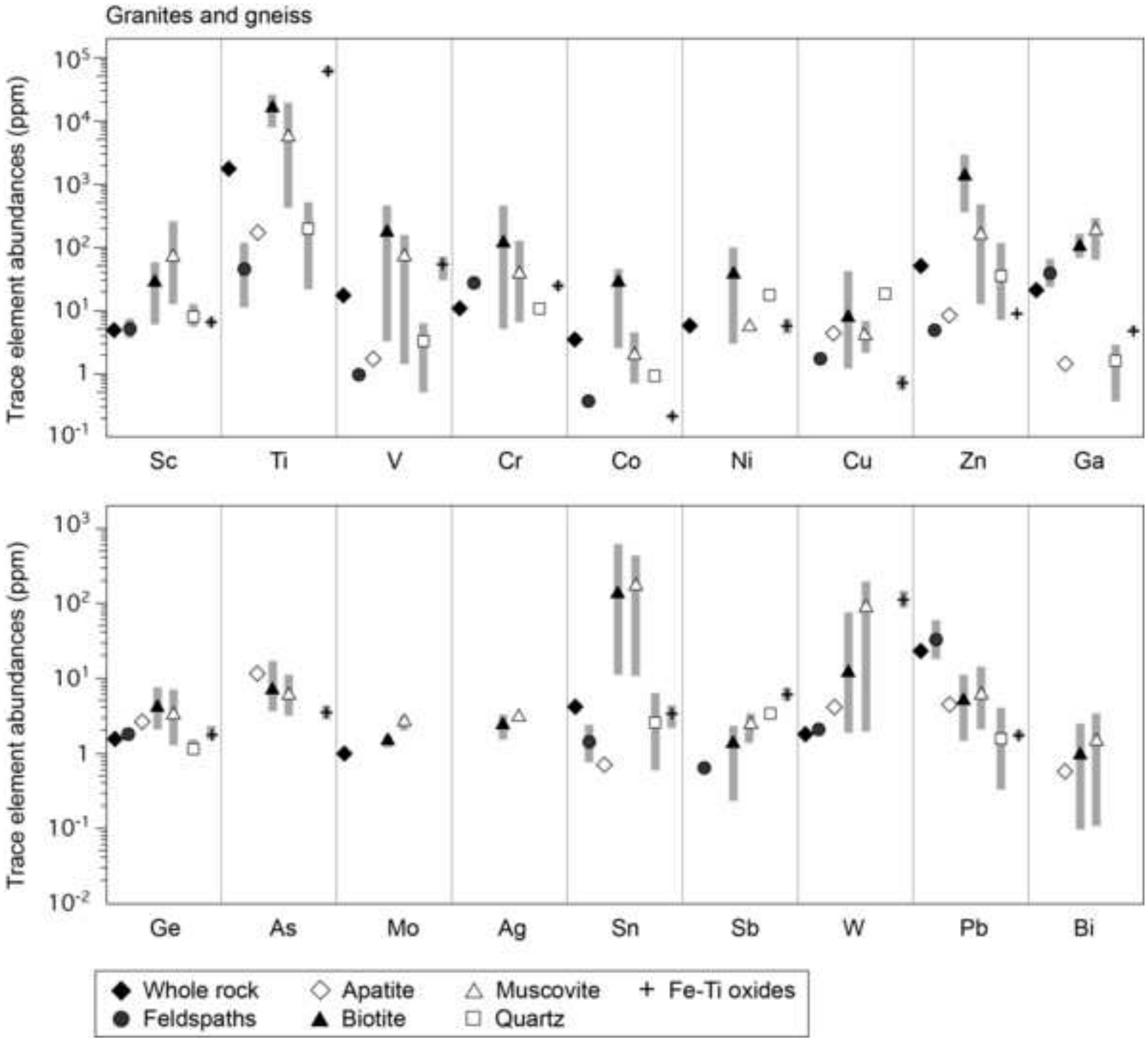

Figure 9 (colour)
Click here to download high resolution image

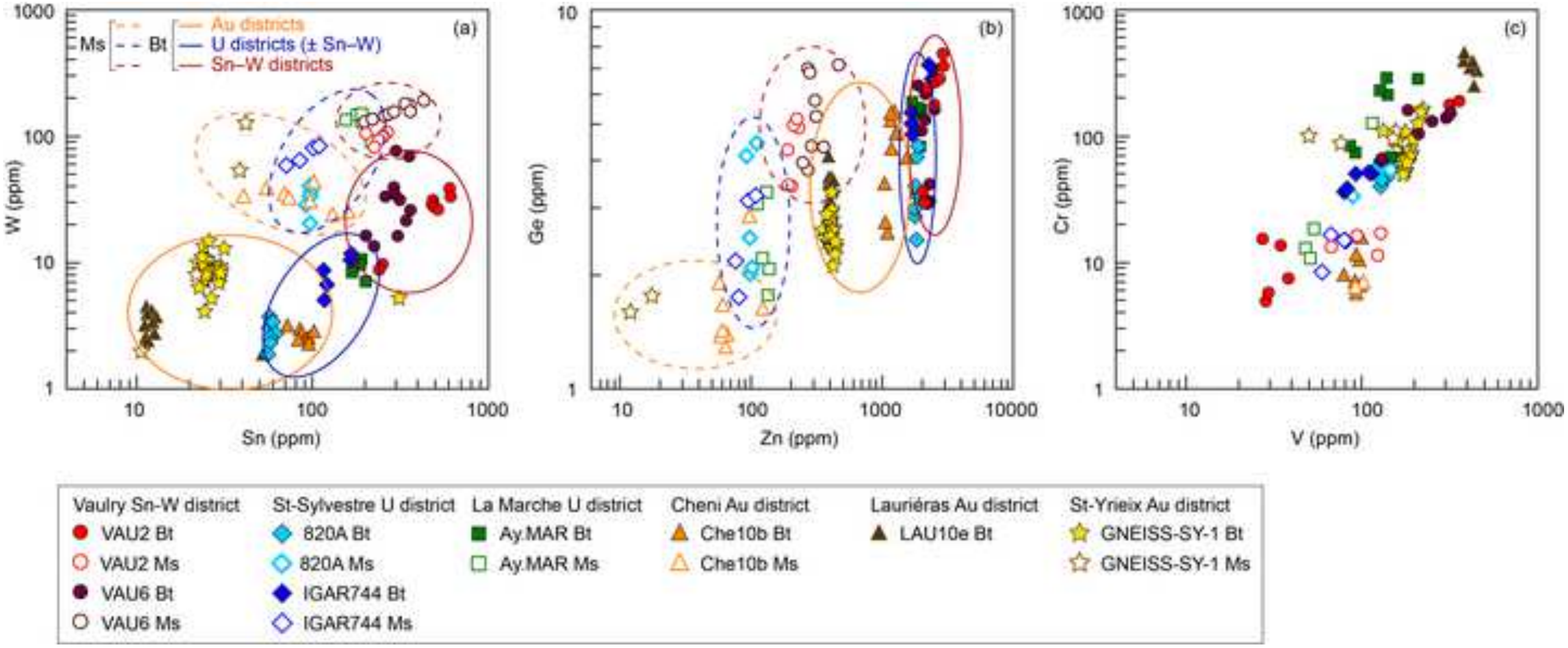

Figure 9 (greyscale)
Click here to download high resolution image

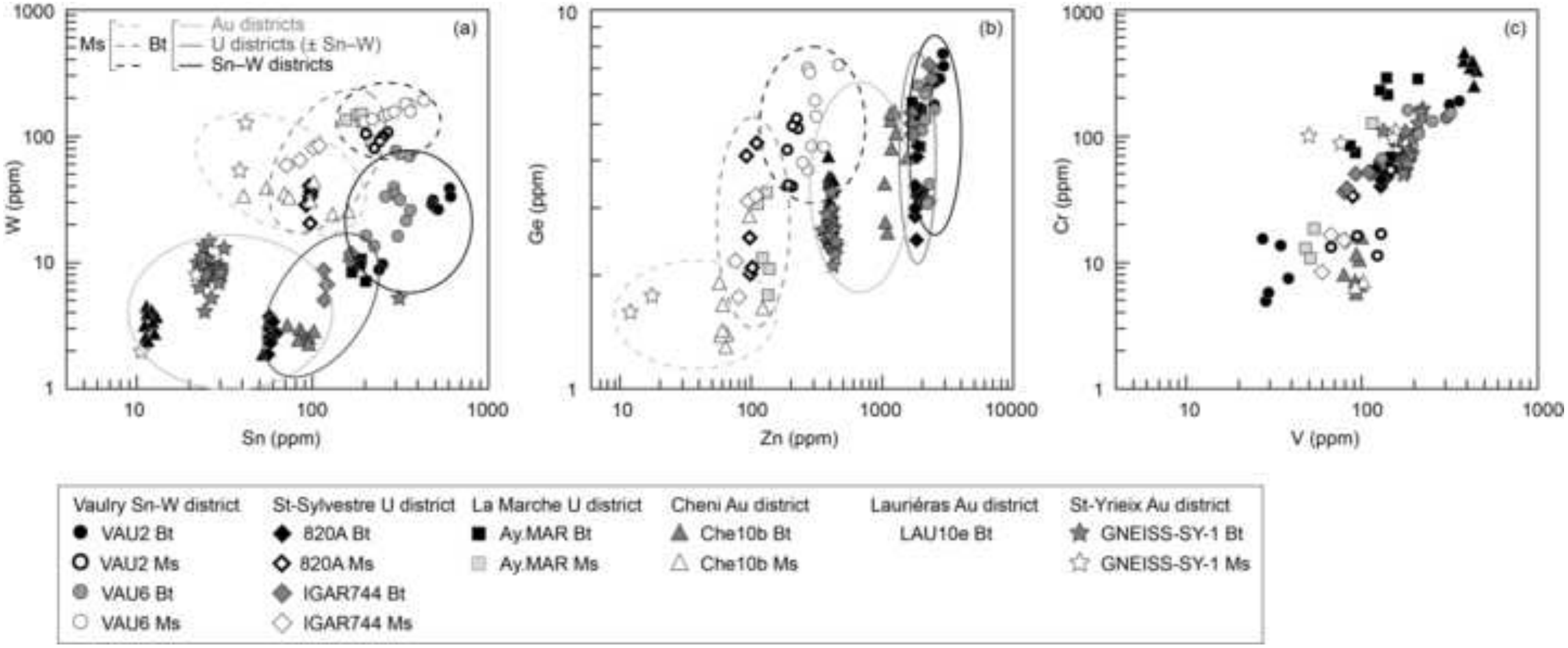

Figure 10 (colour)

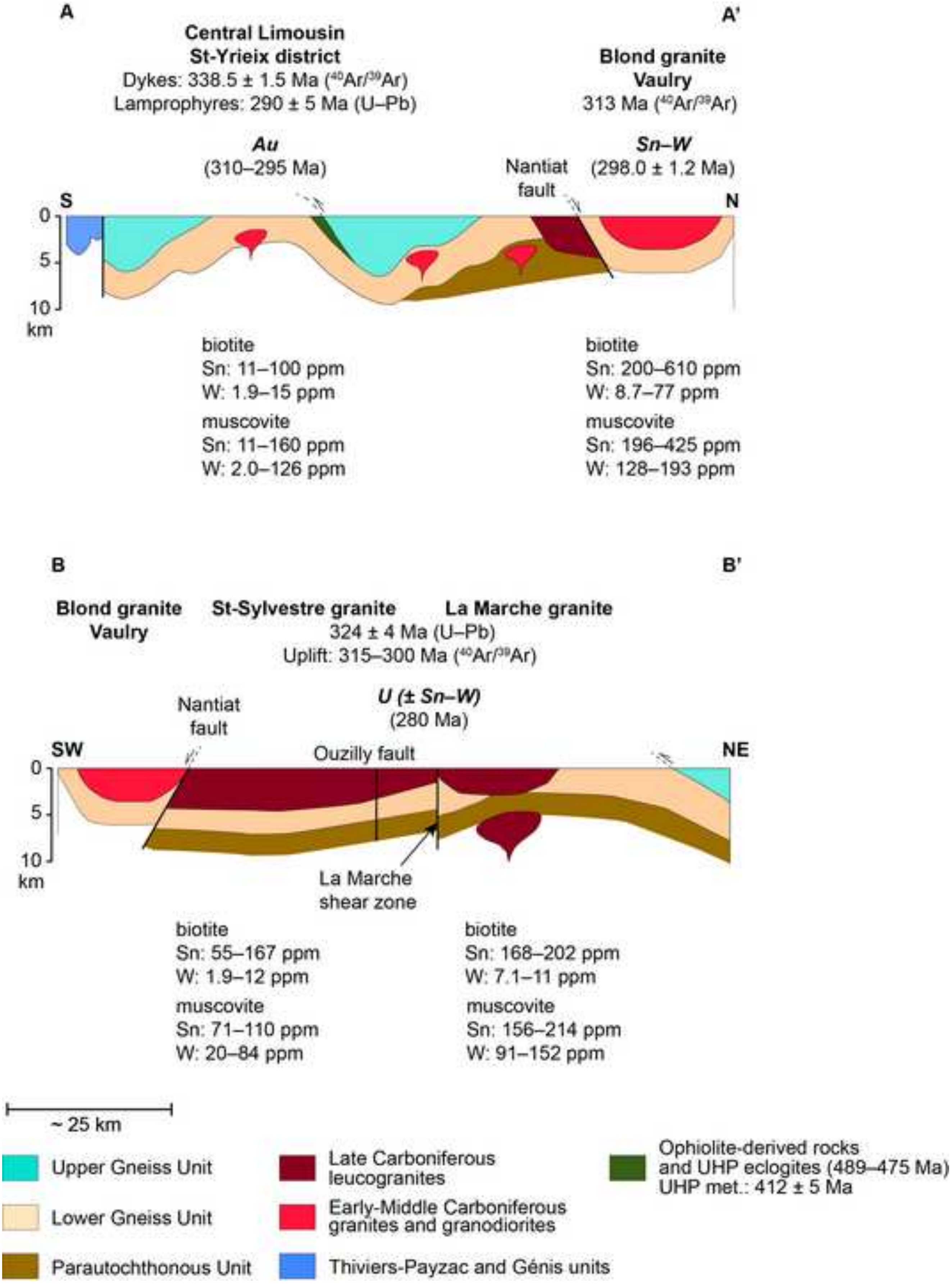

Figure 10 (greyscale)

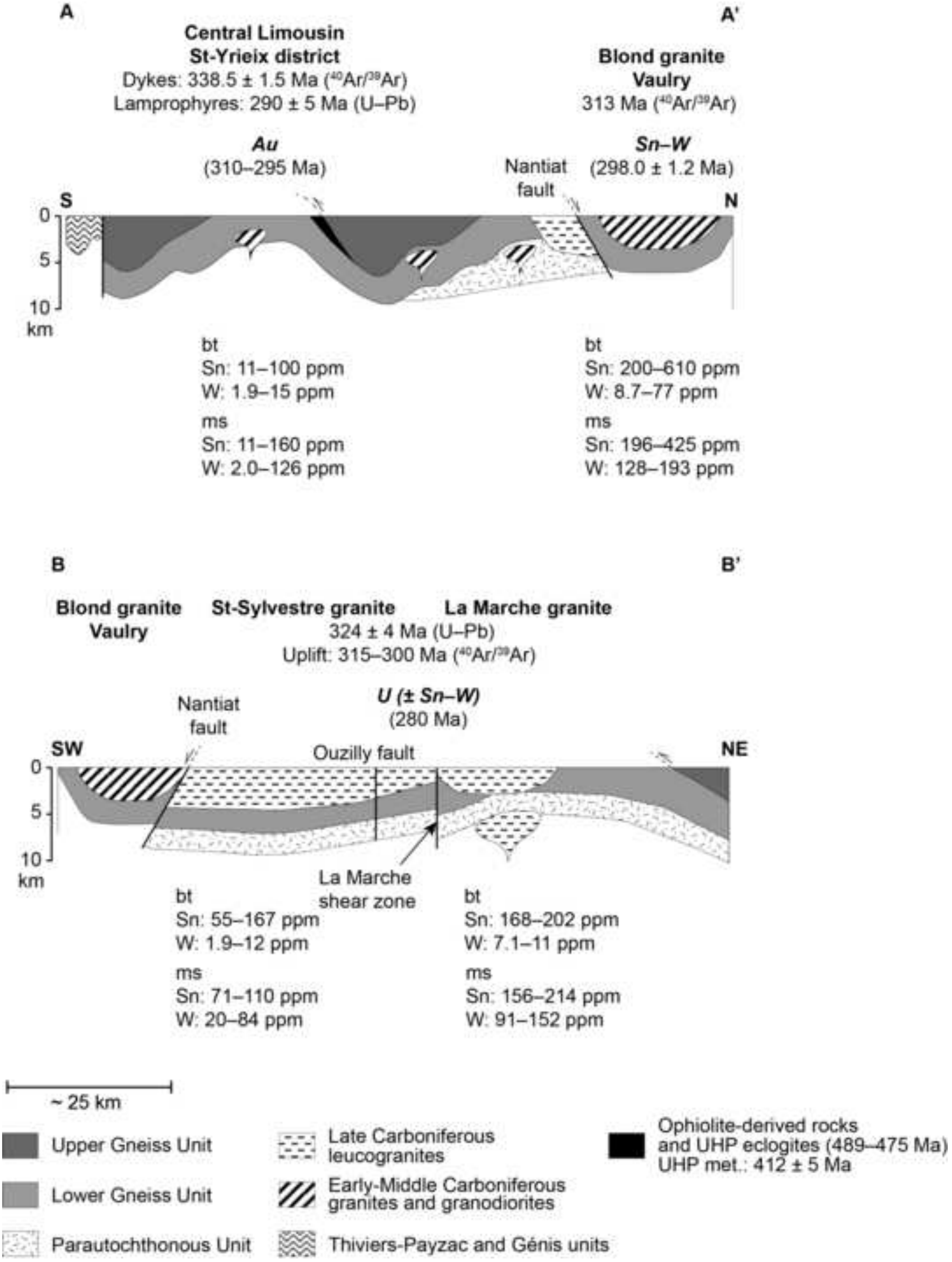

Table 1

Table 1. Description and mineral assemblage of the studied samples

Sample	Rock type	Locality*	Mineralogical assemblage**	Ref.***
LAU-1	Serpentinite	Saint-Laurent	Serp–chl–spl–± ol–± cpx	[1]
LAU-2	Serpentinite	Saint-Laurent	Serp–chl–spl–Fe ox	[1]
CLUZ-6	Serpentinite	Le Cluzeau	Serp–amph–chl–spl–Fe ox– Fe sulph	[1]
FLOT-1	Serpentinite	La Flotte	Serp–amph–chl–± ol–Fe ox	[1]
FLOT-2a	Serpentinite	La Flotte	Serp–spl–ol–Fe ox	[1]
FLOT-2b	Serpentinite	La Flotte	Serp–chl–Fe ox	[1]
CLUZ-1	Amphibolite (metamorphosed dyke)	Le Cluzeau	Amph–plag–chl–Fe ox	[1]
CLUZ-1a	Amphibolite (metamorphosed dyke)	Le Cluzeau	Amph–plag–chl–Fe ox	[1]
CLUZ-4	Amphibolite (metagabbro)	Le Cluzeau	Amph–plag–chl–ttn–Fe ox– Fe sulph	[1]
CLUZ-5	Amphibolite (metagabbro)	Le Cluzeau	Amph–plag–chl–Fe ox	[1]
L04-143	Eclogite	500 m E of Saint-Laurent	Grt–omph–zo–amph–rt–ilm	[2]
VAU2	Leucogranite	Vaulry	Fsp–plag–qtz–bt–ms–zrc	[3]
VAU6	Leucogranite	Vaulry	Fsp–plag–qtz–bt–ms–zrc	[3]
GNEISS-SY-1	Orthogneiss	St-Yrieix	Fsp (mi)–plag (ab)–qtz–bt–ms–ap–zrc	[1]
Lau-10e	Leucogranite	Lauriéras	Fsp (mi)–plag (ab)–qtz–bt–py–Fe-Ti ox–zrc	[4]
Che10b	Leucogranite	Cheni	Fsp (mi)–plag (ab)–qtz–bt–ms–chl–zrc	[5]
IGAR744	Leucogranite	St-Sylvestre	Fsp–plag–qtz–bt–ms–zrc–mz	[6]
820A	Leucogranite	St-Sylvestre	Fsp–plag–qtz–bt–ms–ap–zrc–mz	[6]
Ay.MAR	Leucogranite	La Marche	Fsp–plag–qtz–bt–ms–zrc–mz	[7]

* see Figure 1

** The mineral abbreviations are from Kretz, R. (1983); Fe sulph: Fe-sulphides (pyrite)

*** [1] This study; [2] Berger et al., 2010; [3] Vallance et al., 2001; [4] Essarraj et al., 2001; [5] Vallance et al., 2004; [6] El Jarray, 1993; [7] Ayt Ougougdal, 1993

Table 2

Click here to download Table: ElKorh_Table2.docx

Table 2. Major and trace element composition of the samples from the Limousin ophiolite.

	Serpentinites					Amphibolites				Orthogneiss	Eclogite		OFB
	LAU1	LAU2	CLUZ6	FLOT2a	FLOT2b	CLUZ1	CLUZ1a	CLUZ4	CLUZ5	GNEISS-SY-1	L04-143		Mean (± 2sd)
											[1]	[2]	[3]
SiO_2	38.92	38.62	39.13	35.53	35.39	48.06	46.82	49.23	48.26	74.44	39.50	40.00	
TiO_2	bdl	bdl	0.12	0.06	0.07	0.21	0.22	0.34	0.33	0.30	2.88	2.90	
Al_2O_3	1.89	1.69	4.19	3.30	4.30	18.41	14.83	16.33	16.13	13.10	20.46	20.48	
Fe_2O_3	4.76	5.31	7.30	6.34	6.96	0.85	1.19	0.59	1.02	0.20	0.90	–	
FeO	2.55	1.95	3.61	4.09	3.03	5.18	6.65	4.22	5.99	1.95	16.77	17.57	
MnO	0.10	0.07	0.13	0.15	0.13	0.11	0.15	0.09	0.14	0.03	0.30	0.30	
MgO	36.33	36.06	30.41	37.52	34.74	10.24	13.54	11.11	10.94	0.49	8.32	8.47	
CaO	0.58	0.03	2.86	0.43	0.07	12.43	11.33	13.85	11.74	0.91	8.86	9.06	
Na_2O	0.03	bdl	0.27	bdl	bdl	1.84	1.54	1.42	2.07	2.65	0.72	0.74	
K_2O	bdl	bdl	0.02	bdl	bdl	0.13	0.11	0.12	0.17	4.99	0.06	0.05	
P_2O_5	0.05	bdl	bdl	bdl	bdl	bdl	bdl	bdl	bdl	0.16	bdl	0.07	
LOI	13.60	14.88	11.28	11.62	14.21	1.61	2.39	1.68	2.14	0.62	-1.07	-0.86	
Total	98.81	98.61	99.32	99.04	98.91	99.07	98.75	98.97	98.93	99.83	98.77	100.74	
Ti	bdl	bdl	731	420	378	1247	1289	2014	1978	1774	17285	17381	9035 (5716)
Sc	12	11	23	9.6	8.9	32	39	46	38	4.7	66	–	41 (10)
V	51	40	64	39	36	137	161	172	167	17	213	–	309 (132)
Cr	2793	3042	2436	3427	2837	958	1120	859	906	11	284	280	259 (198)
Co	96	87	114	137	129	42	55	36	47	3.5	37	36	45 (9)
Ni	1826	1992	1326	1883	1850	90	108	216	122	5.6	35	35	105 (83)
Cu	bdl	6.0	119	326	309	48	59	101	78	bdl	34	–	86 (53)
Zn	44	51	81	66	67	39	51	30	43	50	145	–	104 (39)
Ga	1.8	1.6	4.3	3.8	3.7	14	12	12	12	20	17	–	18 (3)
Ge	0.88	0.82	1.2	0.89	0.91	1.2	1.4	1.4	1.4	1.6	2.3	–	1.5 (0.2)
As	bdl	3.7	bdl	bdl	19	bdl	bdl	bdl	3.8	bdl	2.7	–	0.23 (0.52)
Mo	bdl	bdl	bdl	bdl	bdl	bdl	bdl	bdl	bdl	1.02	bdl	–	0.66 (1.22)
Sn	bdl	bdl	bdl	bdl	bdl	bdl	bdl	bdl	bdl	4.2	0.51	–	1.1 (0.8)
Sb	bdl	0.22	bdl	bdl	0.45	bdl	bdl	bdl	0.33	bdl	0.43	–	0.02 (0.03)
W	0.50	0.29	0.83	bdl	1.8	bdl	bdl	0.30	bdl	1.8	14	–	0.07 (0.26)
Pb	bdl	bdl	0.84	bdl	bdl	bdl	0.72	bdl	1.1	23	10	–	0.56 (0.88)
Bi	bdl	bdl	bdl	bdl	bdl	bdl	bdl	bdl	bdl	bdl	0.19	–	0.01 (0.01)
Cs	0.14	0.17	0.17	bdl	bdl	0.21	bdl	0.21	0.43	6.2	0.59	0.60	
Rb	bdl	0.40	0.88	0.45	0.59	1.9	1.7	1.9	2.9	267	4.0	3.7	
Ba	9.4	13	14	8.7	12	23	23	14	27	381	12	12	
Th	bdl	bdl	bdl	bdl	bdl	bdl	bdl	0.10	bdl	12	0.13	0.18	
U	bdl	bdl	bdl	bdl	bdl	bdl	bdl	0.13	bdl	4.0	0.17	0.19	
Nb	0.12	bdl	0.13	bdl	bdl	bdl	bdl	3.1	bdl	10	13	14	
Ta	bdl	bdl	bdl	bdl	bdl	bdl	bdl	0.20	bdl	1.1	1.1	1.1	
La	bdl	bdl	0.18	0.11	0.24	0.47	0.51	0.92	0.50	26	36	38	
Ce	bdl	bdl	0.41	0.21	0.44	1.1	1.3	2.2	1.6	57	68	68	
Pr	bdl	bdl	0.07	0.04	0.08	0.21	0.23	0.40	0.27	6.8	7.7	7.6	
Sr	3.7	bdl	18	2.2	bdl	212	90	153	167	65	371	355	

Nd	bdl	bdl	0.47	0.17	0.38	1.2	1.3	2.1	1.6	25	30	29
Zr	bdl	bdl	2.1	bdl	1.5	3.9	3.6	9.7	6.1	158	157	150
Hf	bdl	bdl	0.09	bdl	0.05	0.16	0.15	0.38	0.27	4.8	4.2	3.8
Sm	bdl	bdl	0.22	0.05	0.13	0.47	0.51	0.83	0.67	5.8	5.8	5.6
Eu	0.009	0.007	0.12	0.05	0.09	0.45	0.45	0.45	0.46	0.70	4.7	4.6
Gd	0.02	0.03	0.33	0.06	0.16	0.66	0.72	1.1	0.93	5.6	5.4	5.2
Tb	0.007	0.006	0.06	0.01	0.03	0.12	0.13	0.22	0.18	1.0	0.79	0.78
Dy	0.07	0.07	0.47	0.09	0.21	0.88	0.96	1.5	1.3	7.0	5.0	4.8
Y	0.60	0.51	2.6	0.61	1.3	4.9	5.3	8.7	7.0	42	29	28
Ho	0.02	0.02	0.11	0.02	0.05	0.20	0.22	0.34	0.29	1.5	1.2	1.0
Er	0.07	0.06	0.30	0.08	0.15	0.54	0.60	0.93	0.77	4.3	3.5	3.2
Tm	0.01	0.01	0.04	0.02	0.03	0.08	0.09	0.14	0.11	0.62	0.56	0.54
Yb	0.11	0.09	0.29	0.13	0.17	0.52	0.58	0.92	0.72	4.0	4.3	4.1
Lu	0.02	0.01	0.05	0.03	0.03	0.08	0.09	0.14	0.11	0.56	0.74	0.71

Major element data are from El Korh et al. (in press)
[1] This study; [2] Berger et al. (2010); [3] Jenner and O'Neill (2002)
2sd: 2σ standard deviation
bdl: below detection limit

Table 3

Click here to download Table: ElKorh_Table3.docx

Table 3. Trace element abundances in the mineral assemblage of serpentinites

	serp LAU2	Fe-serp LAU2	Fe-serp FLOT1	serp FLOT1	serp FLOT2a	Fe-serp FLOT2b	serp FLOT2b	Fe-serp CLUZ6	serp CLUZ6	ol FLOT1	ol FLOT2a	spl LAU2	spl FLOT2a
Sc	3.0–15	4.4–13	2.2–4.3	1.9–6.5	2.3–133	2.9–4.0	2.7–4.0	2.2–5.9	2.2–5.1	3.4–4.7	1.7–6.9	1.5–21	4.53–14
Ti	8.0–27	14–133	12–38	27–107	9.1–7360	21–62	47–98	8.3–42	6.5–79	7.8–19	6.9–8.0	1709–2103	112–410
V	1.6–3.7	3.4–66	0.69–1.0	0.58–1.8	9.7–221	2.4–4.0	2.6–3.9	2.2–6.9	0.53–7.4	bdl	0.85–6.9	1110–1459	388–834
Cr	9.1–100	16–3950	3.9–8.6	3.6	3.6–10209	2.5–8.6	2.5–6.9	2.3–22	5.7–24	8.1	6.01–133	86141–87133	76700–144817
Co	13–83	64–299	26–259	107–275	45–905	96–235	66–115	89–267	70–426	105–332	109–153	139–295	235–1140
Ni	2079–3670	2318–6764	1775–3251	1545–2252	479–3444	2373–4140	2121–2715	1503–3839	1612–4763	2055–4467	1870–2527	1154–8395	949–10686
Cu	4.5–55	4.9–424	8–699	1.3–56	14–1360	78–381	82–333	36–285	21–270	24–386	4.1–157	1.4–76	12–1023
Zn	22–90	25–125	3.7–7.7	4.2–10	5.8–126	22–90	18–45	62–198	17–321	6.5–65	7.5–20	891–1499	1812–2758
Ga	0.31–0.50	0.25–4.6	0.22–0.53	bdl	0.47–3.2	0.44–1.0	0.35–0.86	0.48–1.5	0.24–1.2	0.84–4.3	0.31	5.2–10.60	34–127
Ge	1.1–2.0	1.3–3.1	1.4–2.3	0.62–1.3	1.0–1.6	1.1–2.9	0.86–1.4	1.2–3.3	1.0–1.8	0.36–1.4	0.76–1.6	0.24–2.2	1.4
As	2.7–5.8	4.4–9.3	5.1–12	1.4–6.9	1.3–5.2	19–31	14–19	1.5–5.3	1.4–3.4	3.9–24	3.4–5.6	1.4–8.4	bdl
Mo	bdl	bdl	0.51	bdl	bdl	bdl	bdl	0.35–0.44	bdl	bdl	bdl	bdl	bdl
Ag	bdl	bdl	0.23–0.89	0.48	bdl	0.21–0.24	bdl	0.16–0.20	0.24	0.26	bdl	1.3	bdl
Sn	0.45–0.70	0.40–0.85	0.38–1.1	0.22–0.79	0.36–2.8	0.20–0.37	0.27–0.37	0.22–0.64	0.26–0.48	0.47–0.81	0.28–0.74	0.36–1.8	0.68
Sb	bdl	0.14–0.37	0.13–1.1	bdl	bdl	0.26–0.73	0.22–0.54	0.12–0.19	0.15–0.17	0.18–0.91	bdl	0.42–2.5	1.0
W	0.32–0.68	0.29–0.72	4.3–7.6	1.2–3.9	0.29–1.7	0.49–3.7	0.41–0.72	0.18–7.3	0.23–0.44	0.83	bdl	1.2–2.8	3.4
Au	bdl	bdl	bdl	bdl	bdl	bdl	bdl	bdl	bdl	bdl	bdl	bdl	bdl
Pb	0.49–0.54	0.32–1.4	0.32–0.85	0.27–1.9	0.23–0.26	0.22–0.47	0.25–0.47	0.44–0.93	0.19–1.2	bdl	bdl	0.44–3.0	bdl
Bi	bdl	0.09–0.31	bdl	bdl	0.09–0.51	bdl	bdl	bdl	bdl	bdl	bdl	0.34–1.4	bdl

	spl CLUZ6	chl LAU2	chl FLOT1	chl FLOT2b	chl CLUZ6	amph FLOT1	amph CLUZ6	Fe ox LAU2	Fe ox FLOT1	Fe-Ni ox FLOT1	Fe ox FLOT2a	Fe ox FLOT2b	Fe sulph FLOT2a
Sc	1.6–3.7	10—17	4.0–7.7	4.4–8.6	4.88–18	18—26	22—54	1.8–14	bdl	bdl	8.2	2.1	bdl
Ti	1350–6603	143–168	169–415	155–403	196–449	620–678	808–1808	14–60	46-–175	bdl	bdl	11	bdl
V	234–747	149–188	8.7–73	34–96	51–106	33–60	123–182	15–23	5.1–23	bdl	83	13	9.7
Cr	43357–113080	10044–12280	546–11902	1421–11214	1408–9289	415–4665	1623–4740	855	653–4916	bdl	12263	99	381
Co	64–159	38–46	44–108	26–57	34–64	33–72	52–101	9.7–145	7.7–23	8516	213	764	2127
Ni	199–442	1025–1270	852–1443	494 –1208	573–946	586–902	737–1481	238–3004	81–323	140957	1906	15878	79693
Cu	1.4–47	1.2–7.6	7.0–23	3.49–70	4.6–141	3.0–24	14–176	5.1–25	1692–5508	85822	94	4747	2622
Zn	1178–2361	19–35	6.7–46	13–46	39–74	22–41	61–108	4.7–70	145	2606	90	1624	55
Ga	6.5–15	12–16	1.2–13	5.3–15	9.8–20	1.7–6.6	10–30	1.1	3.1	27	20	11	4.7
Ge	0.26–0.39	1.3–5.1	0.55–1.3	0.33–0.80	0.40–1.1	1.5–1.9	1.5–1.9	bdl	1.1–1.3	1.2	2.1	0.81	bdl
As	bdl	9.2	1.3	2.1–4.7	bdl	4.1–5.3	2.5–8.7	bdl	6.7	232	bdl	206	7.0
Mo	0.34	6.2	bdl	bdl	bdl	bdl	bdl	bdl	bdl	6.6	bdl	bdl	bdl
Ag	bdl	2.9–3.1	bdl	bdl	bdl	bdl	bdl	bdl	bdl	177	bdl	4.1	9.2
Sn	0.24–0.73	0.37–5.8	0.31–1.5	bdl	0.31–1.2	1.1–1.6	0.71–1.3	2.3	bdl	bdl	bdl	bdl	bdl
Sb	bdl	2.7–5.1	0.27	0.18	bdl	bdl	bdl	bdl	bdl	5.6	bdl	7.1	bdl
W	0.2	5.4	1.8	bdl	bdl	0.74–1.3	0.90–3.4	bdl	3.5–4.0	7.5	bdl	7.5	bdl
Au	bdl	bdl	bdl	bdl	bdl	bdl	bdl	bdl	bdl	bdl	bdl	bdl	bdl
Pb	bdl	5.4–5.6	0.33	bdl	bdl	0.26–0.58	0.86	bdl	bdl	31	bdl	40	40
Bi	bdl	3.3–3.6	bdl	bdl	bdl	bdl	0.12	bdl	bdl	2.0	bdl	2.8	4.7

bdl: below detection limit

Table 4

Click here to download Table: ElKorh_Table4.docx

Table 4. Trace element abundances in the mineral assemblage of amphibolites

	amph	amph	amph (± oxidised)	plag	plag	ttn	Fe ox	Fe sulph
	CLUZ1	CLUZ4	CLUZ4	CLUZ1	CLUZ4	CLUZ4	CLUZ1	CLUZ4
Sc	9.8–37	12–82	12–35	2.6–5.8	1.4–4.7	13	bdl	8.0–12
Ti	264–1536	396–3000	345–1069	9.4–239	221–306	150697–184188	14	72–361
V	24–149	28–320	36–116	bdl	3.8–10	225–341	bdl	25–79
Cr	113–736	28–1775	24–335	bdl	bdl	113–522	bdl	30–57
Co	48–65	27–53	40–46	0.29–5.6	0.4–8.3	2.1—20	1285	21–7180
Ni	97–148	97–288	224–709	bdl	28–54	86	7202	114–22078
Cu	1.4–93	6.5–53	9.5–71	2.8–4.7	2.2–28	4.1–30	1017	27763–89963
Zn	49–66	25–51	40–59	bdl	7.6	4.7–34	122	160–449
Ga	8.3–13	2.3–17	3.0–6.6	10–21	13–17	0.79–8.7	bdl	1.6–6.3
Ge	1.2–2.1	1.5–2.7	1.2–2.4	0.79	0.98	3.5–5.4	bdl	bdl
As	bdl	1.3–8.8	1.1–7.2	bdl	bdl	4.2	9.83	36
Mo	bdl	bdl	bdl	bdl	bdl	3.7	bdl	4.2
Ag	bdl	2.1	0.21	bdl	bdl	bdl	6.27	39–99
Sn	0.28–0.97	0.37–1.0	0.22–1.2	bdl	bdl	4.7–5.6	bdl	2.0
Sb	0.37–0.39	0.19–0.65	0.17–0.22	bdl	bdl	0.48	1.08	4.3
W	2.9	bdl	bdl	0.58	bdl	16–18	bdl	bdl
Au	bdl	bdl	bdl	bdl	bdl	bdl	bdl	bdl
Pb	bdl	bdl	0.29	0.67–15	0.46–0.70	bdl	7.09	8.67–28
Bi	bdl	bdl	bdl	bdl	bdl	0.41	bdl	1.2–8.5

bdl: below detection limit

Table 5

Table 5. Trace element abundances in the mineral assemblage of the UHP zoisite-elcogite

	garnet L04-143	omphacite L04-143	zoisite L04-143	rutile L04-143	amphibole L04-143	ilmenite L04-143
Sc	35–65	37–42	18–51	4.3–69	27–59	15–54
Ti	56–13793	255–287	172–230	599343	1020–9465	377586
V	56–132	585–811	353–986	2625–2969	333–556	648–903
Cr	33–281	305–498	166–329	1586–2006	286–394	450–720
Co	34–42	12–20	6.9–19	0.70–27	17–67	62–67
Ni	8.0	67–115	10–25	30	68–240	102–147
Cu	bdl	89	16–17	9.9–13	16–21	bdl
Zn	50–176	57–192	20–46	17–119	81–200	74–106
Ga	7.4–16	28–41	111–186	9.5	21–32	4.8
Ge	2.7–3.4	1.6–2.6	8.8–19	3.6	3–21	6.3
As	bdl	7.5–8.7	13–22	6.3–11	7.8–11	bdl
Mo	bdl	4.7	5.3–15	4.2–8.3	9.0–16	bdl
Ag	bdl	bdl	7.1–11	bdl	3.7–14	bdl
Sn	0.82	1.5–1.6	2.8–20	13–17	1.1–23	3.8
Sb	bdl	1.5–2.3	12–16	5.0–13	1.2–20	3.1
W	5.7	3.1	10–16	111–164	8.6–10	17–85
Au	bdl	bdl	bdl	bdl	bdl	bdl
Pb	bdl	6.1–21	75–98	12	16–39	bdl
Bi	bdl	bdl	5.9–16	bdl	9.6–17	bdl

bdl: below detection limit

Table 6

Table 6. Trace element abundances in the mineral assemblage of granites and gneiss

	bt VAU2	bt VAU6	bt 820A	bt IGAR744	bt Ay.MAR	bt GNEISS-SY-1	bt LAU10e	bt Che10b	ms VAU2	ms VAU6	ms 820A
Sc	5.8–51	9.3–55	15–19	9.5–16	15–25	26–58	50–58	17–31	55–255	14–24	35–41
Ti	7976–21870	10293–19763	20053–21382	18693–26499	16176–17570	13261–18489	9905–13156	12883–20178	3873–5036	1744–19323	5771–8918
V	27–356	3.1–317	123–152	79–127	84–206	132–216	374–447	78–105	10–127	1.4–21	38–146
Cr	5.0–189	66–160	41–62	37–65	68–285	49–161	246–449	5.7–16	11–17	bdl	33–54
Co	2.5–35	7.3–19	34–39	20–43	16–21	32–37	29–45	24–36	1.4–2.7	2.0–3.0	1.8–4.3
Ni	3.0–39	11–20	27–34	15–24	28–39	32–69	84–98	7.6–14	bdl	bdl	bdl
Cu	1.5–9.3	1.6–42	bdl	bdl	bdl	1.2	bdl	1.4	4.5	2.2–6.6	bdl
Zn	1956–2902	1883–2527	1784–1914	1667–2375	1699–1985	352–441	389–434	1038–1541	191–234	252–466	92–112
Ga	67–147	80–139	93–106	89–133	76–93	68–88	141–164	97–141	221–282	157–205	179–192
Ge	3.1–7.7	3.1–7.0	2.5–4.4	4.7–7.1	4.4–5.7	2.1–3.3	3.1–4.1	2.6–5.3	3.4–5.2	3.8–7.2	2.0–4.5
As	3.7–5.8	4.2–5.3	4.9	bdl	bdl	17	bdl	9.0–10	bdl	11	bdl
Mo	bdl	1.2	bdl	bdl	bdl	bdl	bdl	1.7	bdl	2	3.2
Ag	bdl	bdl	bdl	bdl	bdl	1.5–3.3	bdl	bdl	bdl	bdl	3.1
Sn	238–610	200–359	55–62	115–167	168–202	22–32	11–13	52–100	202–267	196–425	92–98
Sb	bdl	bdl	bdl	bdl	bdl	0.24–0.57	bdl	1.2—2.3	bdl	bdl	1.4–3.4
W	8.7–38	14–77	1.9–3.7	5.1–12	7.1–11	4.0–15	2.4–4.4	1.9–3.2	80–107	128–193	20–40
Au	bdl	bdl	bdl	bdl	bdl	bdl	bdl	bdl	bdl	bdl	bdl
Pb	2.5–8.6	2.6–6.8	3.4–5.5	4.5–8.4	4.3–5.9	1.5–8.6	6.6-9.6	4.4–11	2.2–4.2	2.1–4.7	5.7–14
Bi	bdl	0.53–2.5	bdl	bdl	0.44–0.84	0.10–0.11	bdl	0.9	bdl	2	3.4

	ms IGAR744	ms Ay.MAR	ms GNEISS-SY-1	ms Che10b	mc GNEISS-SY-1	ab GNEISS-SY-1	ap GNEISS-SY-1	qtz GNEISS-SY-1	qtz Che10b	Fe-Ti ox LAU10e
Sc	34–52	41–87	12–86	52–72	6.1– 7.1	3.6– 4.5	bdl	5.5–8.8	12	5.5–7.5
Ti	5129–7281	3914–5082	417–6312	5243–6509	29	11–117	170	21–512	395	53470–72894
V	59–80	34–113	50–153	82–115	bdl	0.96	1.7	0.49–4.2	6.1	30–70
Cr	8.4–16	11–127	87–109	6.3–6.9	bdl	27	bdl	bdl	11	20–28
Co	1.2–2.0	1.1–1.5	1.1–1.6	0.69–2.4	bdl	0.33–0.37	bdl	bdl	0.91	0.19–0.23
Ni	bdl	bdl	5.3	bdl	bdl	bdl	bdl	bdl	18	4.1–7.1
Cu	bdl	bdl	2.1	bdl	bdl	1.7	4.2	bdl	18	0.53–0.92
Zn	78–110	112–137	12–23	58–123	bdl	4.7	8.1	7.0–8.4	114	8.2–9.1
Ga	135–188	157–184	61–138	189–221	62–64	23–25	1.4	0.36–1.9	2.8	4.4–5.4
Ge	1.8–3.2	1.8–3.3	1.6–1.8	1.3–2.9	1.5–1.7	1.7–2.2	2.6	0.96–1.5	bdl	1.5–2.3
As	bdl	bdl	3.1–3.2	bdl	bdl	bdl	12	bdl	bdl	2.8–4.4
Mo	bdl	bdl	bdl	bdl	bdl	bdl	bdl	bdl	bdl	bdl
Ag	bdl	bdl	bdl	bdl	bdl	bdl	bdl	bdl	bdl	bdl
Sn	71–110	156–214	11–42	41–160	2.1–2.4	0.76–1.3	0.7	0.59–0.90	6.3	2.1–4.3
Sb	bdl	bdl	bdl	bdl	bdl	0.64	bdl	bdl	3.4	5.0–7.6
W	59–84	91–152	2.0–126	24–43	bdl	bdl	4.2	bdl	bdl	87–147
Au	bdl	bdl	bdl	bdl	bdl	bdl	bdl	bdl	bdl	bdl
Pb	3.1–6.8	2.2–4.4	2.6–3.5	11–14	51–58	18–22	4.4	0.33–0.35	4	1.5–2.0
Bi	bdl	bdl	0.11–0.20	bdl	bdl	bdl	0.58	bdl	bdl	bdl

bdl: below detection limit